Draft version October 6, 2023
Typeset using LaTeX **twocolumn** style in AASTeX631

The APO-K2 Catalog. I. ~7,500 Red Giants with Fundamental Stellar Parameters from APOGEE DR17 Spectroscopy and K2-GAP Asteroseismology

Jessica Schonhut-Stasik,[1,*] Joel C. Zinn,[2,3,†] Keivan G. Stassun,[1] Marc Pinsonneault,[4] Jennifer A. Johnson,[4,5] Jack T. Warfield,[6] Dennis Stello,[7,8,9,10] Yvonne Elsworth,[11,12] Rafael A. García,[13] Savita Mathur,[14,15] Benoit Mosser,[16] Marc Hon,[17] Jamie Tayar,[18] Guy S. Stringfellow,[19] Rachael L. Beaton,[20,21] Henrik Jönsson,[22] and Dante Minniti[23,24,25]

[1] Vanderbilt University, Department of Physics & Astronomy, 6301 Stevenson Center Ln., Nashville, TN 37235, USA
[2] Department of Astrophysics, American Museum of Natural History, Central Park West at 79th Street, New York, NY 10024, USA
[3] Department of Physics and Astronomy, California State University, Long Beach, Long Beach, CA 90840, USA
[4] Department of Astronomy, The Ohio State University, McPherson Laboratory, 140 W 18th Ave, Columbus, OH 43210, USA
[5] Center for Cosmology and AstroParticle Physics, Physics Research Building, 190 West Woodruff Ave, Columbus, OH 43210, USA
[6] Department of Astronomy, The University of Virginia, 530 McCormick Road, Charlottesville, VA 22904, USA
[7] School of Physics, University of New South Wales, NSW 2052, Australia
[8] Sydney Institute for Astronomy (SIfA), School of Physics, University of Sydney, NSW 2006, Australia
[9] ARC Centre of Excellence for All Sky Astrophysics in 3 Dimensions (ASTRO 3D), Australia
[10] Stellar Astrophysics Centre, Department of Physics and Astronomy, Aarhus University, DK-8000 Aarhus C, Denmark
[11] Stellar Astrophysics Centre, Department of Physics and Astronomy, Aarhus University, Ny Munkegade 120, DK-8000 Aarhus C, Denmark
[12] School of Physics and Astronomy, University of Birmingham, Edgbaston, Birmingham, B15 2TT, UK
[13] Université Paris-Saclay, Université Paris Cité, CEA, CNRS, AIM, 91191, Gif-sur-Yvette, France
[14] Instituto de Astrofísica de Canarias (IAC), E-38205 La Laguna, Tenerife, Spain
[15] Universidad de La Laguna (ULL), Departamento de Astrofísica, E-38206 La Laguna, Tenerife, Spain
[16] LESIA, Observatoire de Paris, Université PSL, CNRS, Sorbonne Université, Université de Paris, 92195 Meudon, France
[17] Institute for Astronomy, University of Hawai‘i, 2680 Woodlawn Drive, Honolulu, HI 96822, USA
[18] Department of Astronomy, University of Florida, Bryant Space Science Center, Stadium Road, Gainesville, FL 32611, USA
[19] Center for Astrophysics and Space Astronomy, University of Colorado at Boulder, 389 UCB, Boulder, CO 80309-0389, USA
[20] Space Telescope Science Institute, Baltimore, MD, 21218, USA
[21] Department of Physics and Astronomy, Johns Hopkins University, Baltimore, MD 21218, USA
[22] Materials Science and Applied Mathematics, Malmö University, SE-205 06 Malmö, Sweden
[23] Departamento de Fisica, Universidade Federal de Santa Catarina, Trinidade 88040-900, Florianopolis, Brazil
[24] Instituto de Astrofísica, Facultad de Ciencias Exactas, Universidad Andres Bello, Av. Fernández Concha 700, Santiago, Chile
[25] Vatican Observatory, V00120 Vatican City State, Italy

ABSTRACT

We present a catalog of fundamental stellar properties for ~7,500 evolved stars, including stellar radii and masses, determined from the combination of spectroscopic observations from the Apache Point Observatory Galactic Evolution Experiment (APOGEE), part of the Sloan Digital Sky Survey IV (SDSS), and asteroseismology from K2. The resulting APO-K2 catalog provides spectroscopically derived temperatures and metallicities, asteroseismic global parameters, evolutionary states, and asteroseismically-derived masses and radii. Additionally, we include kinematic information from *Gaia*. We investigate the multi-dimensional space of abundance, stellar mass, and velocity with an eye toward applications in Galactic archaeology. The APO-K2 sample has a large population of low metallicity stars (~288 at $[\mathrm{M/H}] \leq -1$), and their asteroseismic masses are larger than astrophysical estimates. We argue that this may reflect offsets in the adopted fundamental temperature scale for metal-poor stars rather than metallicity-dependent issues with interpreting asteroseismic data. We characterize the kinematic properties of the population as a function of α-enhancement and position in the disk

Corresponding author: Jessica Schonhut-Stasik
jessica.s.stasik@vanderbilt.edu

and identify those stars in the sample that are candidate components of the *Gaia-Enceladus* merger. Importantly, we characterize the selection function for the APO-K2 sample as a function of metallicity, radius, mass, $\nu_{\rm max}$, color, and magnitude referencing Galactic simulations and target selection criteria to enable robust statistical inferences with the catalog.

1. INTRODUCTION

Galactic archaeology probes the Galaxy's stars as a fossil record, investigating their histories to determine the formation and evolution of the Milky Way. Studying these fossils is best achieved using extensive data sets — that well represent the Galaxy's stellar population — over a broad parameter space comprising stellar ages, abundances, and kinematics; this data reveals the *when*, *what*, and *where* of the Milky Way's formation. The gathering of these datasets has grown considerably in the last decade, with a stream of space- and ground-based telescopes providing asteroseismic, spectroscopic, and kinematic measurements determining the ages, compositions, and positions of hundreds of thousands of stars. These data have enabled increasingly detailed descriptions of the Milky Way's stellar building blocks.

In terms of stellar targets, red giant stars are particularly beneficial for Galactic archaeology (e.g., Stello et al. 2015). Due to their high luminosities, red giant stars can be seen to greater distances than less evolved stars, providing a better understanding of the edge of our Galaxy. Furthermore, their solar-like oscillations can be observed in a longer cadence than that which is necessary to observe similar oscillations in dwarfs and subgiants. Asteroseismic, spectroscopic, and kinematic catalogs of giant stars already exist for various samples. CoRoT (Baglin et al. 2006), *Kepler* (Borucki et al. 2010), K2 (Howell et al. 2014) and TESS (Ricker et al. 2014) have been transformational for taking the once-boutique field of asteroseismology into the era of large data sets. There are now large catalogs of asteroseismic data for red giants available from *Kepler* (with ∼16,000 stars from Yu et al. 2018, see also Pinsonneault et al. (2018)), K2 (∼19,000; Zinn et al. (2022)) and TESS (∼158,000; Hon et al. (2021) and ∼1,700; Mackereth et al. (2021)). Spectroscopic data for millions of stars from large-scale surveys such as APOGEE (Majewski et al. 2017), GALAH (Buder et al. 2021), and LAMOST (Cui et al. 2012) complement asteroseismic data by providing the temperatures and metallicities needed for detailed stellar physics and Galactic archaeology studies. To these survey data, *Gaia* (Gaia Collaboration et al. 2016) has also been ground-breaking in adding precise kinematic information for over one billion stars. Here, we present a catalog at the intersection of a subset of these surveys, drawing together asteroseismology from K2; spectroscopy from APOGEE; and kinematics from *Gaia*, and demonstrate its unique potential for stellar physics and Galactic archaeology applications.

We can learn *when* stellar populations formed in our Galaxy using precise asteroseismic stellar ages (e.g., Miglio et al. 2009; Sharma et al. 2016; Silva Aguirre et al. 2018; Rendle et al. 2019; Mackereth et al. 2020). Such age estimates rely on asteroseismic masses in combination with stellar models, metallicities, and temperatures. When performing population asteroseismology on large samples of solar oscillators, it is common to reduce the dimensionality of the oscillation pattern by using two global seismic parameters for faster processing instead of performing detailed mode-by-mode analysis on all targets. These asteroseismic global parameters are the large frequency separation ($\Delta\nu$; related to the mean density) and the frequency of maximum power ($\nu_{\rm max}$; related to log(g) and $T_{\rm eff}$) (Kjeldsen & Bedding 1995; Brown et al. 1991). These global parameters can, in turn, provide the input to calculate high-precision stellar masses and radii using scaling relations (see Section 2.2). These scaling relations, and resulting ages, depend explicitly on temperature measurements; therefore, spectroscopic surveys provide a powerful complement to time-domain asteroseismology.

Spectroscopic data measures stellar abundances, powerfully describing *what* the Galaxy's stellar composition is. An example of the symbiosis between asteroseismic and spectroscopic measurements is the study of the distribution of α-element abundances. As stars formed in our Galaxy, the proportion of metals increased through a series of supernovae, providing an increasingly metal-rich medium for star formation and altering the proportions of α elements to other elements (hereafter, [α/Fe]) (e.g., Burbidge et al. 1957; Timmes et al. 1995). Therefore, the most metal-poor old stars present an excellent probe of the nucleosynthesis pathways in the early Galaxy.

A major prediction from early models is a single-valued function of the α elements as a function of [Fe/H] (e.g., Gilmore et al. 1989). However, with the support of spectroscopic measurements, data have shown

* Neurodiversity Inspired Science and Engineering Graduate Fellow.

† NSF Astronomy and Astrophysics Postdoctoral Fellow.

a double-valued function (Fuhrmann 1998; Prochaska et al. 2000; Bensby et al. 2003), even in the Galactic bar (Queiroz et al. 2021). There are many proposed mechanisms for this [α/Fe]-[Fe/H] bimodality, such as radial migration (Sellwood & Binney 2002; Schönrich & Binney 2009; Nidever et al. 2014; Weinberg et al. 2017; Sharma et al. 2021), two separate episodes of star formation (Chiappini et al. 1997; Haywood et al. 2016; Lian et al. 2020), and stars forming throughout the Galaxy in clumpy bursts (Clarke et al. 2019). Adding asteroseismic ages provides further information, allowing us to test models of the [α/Fe]-[Fe/H] bimodality thanks to their precision, large sample sizes, and a relatively large range of distances compared to isochronal aging techniques. Samples from *Kepler*, K2, and *TESS* are promising for continued work to constrain these models (e.g., Silva Aguirre et al. 2018; Rendle et al. 2019; Mackereth et al. 2019a; Warfield et al. 2021).

With stellar position and orbital parameters derived from astrometry, we can determine *where* stars formed and to which Milky Way component they belong (the halo, thick disk, thin disk, or bulge), separate out populations such as globular clusters Kruijssen et al. (2019); Massari et al. (2019); Forbes (2020); Pérez-Villegas et al. (2020); Callingham et al. (2022) and determine if the stars originated as part of an accretion event by considering the Galactic halo. As the Milky Way developed its structure, it accreted much smaller galaxies, and in some cases, the Milky Way is still actively accreting. For example, the tidal disruption of the Sagittarius dwarf galaxy is ongoing (Ibata et al. 1994; Limberg et al. 2023), the Magellanic Clouds appear to be on their first infall (Besla et al. 2007), and there are dozens of globular cluster streams currently encircling our Galaxy (Bonaca et al. 2020). These accreted bodies come with unique kinematic profiles, and they share integrals of motion (Helmi & de Zeeuw 2000; Font et al. 2011; Simpson et al. 2019) even several billion years later, allowing us, in some cases, to identify their stellar components. These stars also share chemical abundance values, aiding in their identification (Freeman & Bland-Hawthorn 2002; Venn et al. 2004; Lee et al. 2015; Grunblatt et al. 2021).

Combining the abundances, masses, radii, velocities, and positions of evolved stars allows us to assemble a catalog containing the essential data to address the significant questions in Galactic archaeology. Furthermore, combining these parameters can improve the precision of other diagnostic criteria. For example, evolutionary states can be inferred to higher precision by correlating spectroscopic properties with asteroseismic evolutionary (Jönsson et al. 2020), as it is otherwise difficult to separate shell H-burning Red Giant Branch (RGB) stars from core He-burning Red Clump (RC) stars. It is also challenging to infer parameters for red giant branch (RGB) stars, such as ages, with spectroscopic information alone (e.g., Soderblom 2010).

Another problem our extensive data set can explore is a purported conflict between astrophysical priors and asteroseismic masses for low-metallicity halo stars (Epstein et al. 2014), first identified in early *Kepler* data (Pinsonneault et al. 2014). Although more recent investigations have called this result into question (Sharma et al. 2016; Miglio et al. 2016; Valentini et al. 2019), others have supported an inflation of the metal-poor asteroseismic mass scale (Zinn et al. 2019a; Matsuno et al. 2021). With a larger sample of asteroseismic, metal-poor stars available in K2 compared to Kepler, the catalog presented here is a timely addition to this debate.

Our catalog introduces the first APOGEE and K2 combination and includes the incorporation of *Gaia* DR3 data. Because the K2 fields sample very different populations from those seen in the original *Kepler* field, we can gain powerful insights into the formation history of the Milky Way. This paper presents the results from the dedicated targeting efforts of SDSS-IV (Beaton et al. 2021) to observe the K2 fields. The resulting APO-K2 catalog contains the combined data sets for 7,672 evolved Milky Way stars, combining spectroscopic (APOGEE DR17, Abdurro'uf et al. 2021), asteroseismic (K2-GAP, Stello et al. 2015), and astrometric (*Gaia* DR3, Gaia Collaboration et al. 2023) data, with a well-understood selection function (Sharma et al. 2022, hereafter S22). In Section 2, we discuss the data and construction of the catalog. Section 3 presents the final sample, including a discussion of metallicity, the selection function, and a comparison between the APO-K2 and APOKASC-2 (Pinsonneault et al. 2018) samples. In Section 4, we investigate stellar masses in the low metallicity regime, the kinematic properties, and the [α/Fe]-[Fe/H] bimodality as seen in the data set; we also identify halo stars and potential GES members (Helmi et al. 2018; Mackereth et al. 2019b). Section 5 presents the conclusions. The publication of asteroseismic ages for this sample will follow in a companion paper (Warfield et al. in prep.), as will a detailed analysis of sample abundances and multiplicity (Schonhut-Stasik et al. in prep.).

2. SAMPLE DATA

Our catalog uses asteroseismic data from the K2 Galactic Archaeology Program (K2-GAP DR3, Zinn et al. 2022), spectroscopic data from APOGEE DR17 (Abdurro'uf et al. 2021), and astrometric data from

Gaia DR3 (cross-matched from EDR3, included in the APOGEE DR17 release (Abdurro'uf et al. 2021)). Our initial sample is compiled by cross-matching K2-GAP DR3 with APOGEE DR17 (Section 2.1). Having combined these sources we calculated fundamental asteroseismic parameters (Section 2.2), incorporated spectroscopic parameters (Section 2.3), and collated astrometric values (Section 2.4), resulting in the APO-K2 catalog.

2.1. *Cross-match*

The K2-GAP DR3 catalog is the base of our cross-match, which has been analyzed in various works (Stello et al. 2017; Zinn et al. 2020, 2022). The complete list of K2-GAP targets observed by K2 contains 121,715 stars. From here, a cross match with APOGEE DR17 was performed. Around 32% of the K2-GAP stars were also observed in APOGEE (39,319 stars); by then cross-matching those stars with asteroseismic measurements, we have a sample of 8,581 stars (7% of those observed for K2-GAP).

The primary axis for our cross-match between the K2-GAP and APOGEE DR17 catalogs is their associated 2MASS IDs, which come from the Ecliptic Plane Input Catalog (EPIC, Huber et al. 2016), compiled to support target selection and management for the K2 mission. Prior to the match, we sort the APOGEE DR17 targets by signal-to-noise ratio (SNR), dropping the rows with lower SNR where multiple entries for the same target are available. We also only consider APOGEE targets that have a metallicity measurement. Dropping low SNR entries ensures that each entry in the K2-GAP catalog receives a single spectroscopic match, with the highest available SNR observation. To show which stars were dropped, we created a flag for the cross-match (`apo_crossmatch_flag`) and set the value to `1` where no drop was made and `0` otherwise. A minority of stars were observed in multiple K2 campaigns (10% of the sample), and are noted in the final catalog as having observations in multiple campaigns. *Gaia* EDR3 data is already in the APOGEE DR17 table, and so no stars are dropped by adding this information, which was later updated to include DR3 values.

2.2. *Asteroseismic Data*

Asteroseismic detections for thousands of stars became possible with missions such as CoRoT (Auvergne et al. 2009; De Ridder et al. 2009) and *Kepler* (Huber et al. 2009; Stello et al. 2013). However, these missions had limited sky coverage, selecting stars primarily for planet-hunting (Sharma et al. 2016, 2017). In *Kepler*, this resulted in only a fraction of the available oscillating targets observed, at a given combination of age, metallicity, and distance (Silva Aguirre et al. 2018).

The *Kepler* mission targeted a field in the Cygnus and Lyra constellations, with a four-year nominal mission, to find Earth-like planets around Sun-like stars. Conveniently, *Kepler's* precise photometry also allowed for the study of asteroseismic variability in thousands of cool stars; the long cadence of *Kepler* being particularly advantageous, with 29.4-minute observations ideal for studying the oscillation periods of red giants (e.g., Bedding et al. 2010).

Following the failure of the second of *Kepler's* four reaction wheels in May 2013, the *Kepler* spacecraft began on a second mission, K2. The spacecraft was repurposed using solar wind for partial stabilization, allowing the telescope to continue to observe, although the acquisition of *Kepler's* original field was no longer possible due to the lack of stable pointing. Therefore, unlike the fixed original field, K2 observed 18 regions across a 360° ecliptic field of view for ∼80 days at a time (Howell et al. 2014). Each K2 campaign covers 115.64 sq. deg. — over 21 CCD modules, each made of 1024 × 2200 pixel CCDs (2″.98 pixel scale); there are slight gaps between the CCDs and between each of the 21 modules.

The K2 mission had several scientific objectives proposed through guest observer programs. The international collaboration of K2-GAP (Stello et al. 2015) created a dedicated program to target red giants far beyond the solar neighborhood, which provided a trove of new asteroseismic data by detecting oscillations, with an aim to study the formation and evolution of the Milky Way. Roughly 25% of the observed K2 targets were allocated to K2-GAP.

K2 performed 18 full observing campaigns before a lack of fuel forced retirement in 2018. In Zinn et al. (2022, hereafter Z22), the authors present K2-GAP for campaigns (C) C1-C8 and C10-C18[1]. The Z22 catalog represents the largest asteroseismic sample of red giants, with both ν_{max} and $\Delta\nu$, in the literature to date.

Our catalog includes K2-GAP asteroseismic data from C1-C8 and C10-C18, and was analysed by members of

[1] Some differences between campaigns are worth noting: C3 had a slightly shifted field of view due to a late change in roll angle; therefore, some of the proposed targets were unobservable. During C10, a permanent failure of one of the CCD modules occurred, resulting in stars in this, and all subsequent campaigns, being observed partially, or not at all. C18 has very few seismic detections. C9 was not used as it was a dense field chosen for microlensing, nor C19, which had very few asteroseismic detections due to its short duration.

the *Kepler* Asteroseismic Science Consortium (KASC)[2]. The K2-GAP lightcurves were reduced and calibrated in a manner appropriate for asteroseismology (see Z22, where the interested reader can find a full explanation). Briefly, each star in the sample received analysis from six independent pipelines, which returned asteroseismic parameters. The final asteroseismic values are the average of the pipeline values, with an outlier rejection algorithm applied. For the stars observed in multiple campaigns, a weighted average of the averaged pipeline values from each campaign serves as the final set of parameters.

The final two asteroseismic parameters in the APO-K2 catalog are the frequency of maximum oscillation power ($\nu_{\rm max}$) and the large frequency separation ($\Delta\nu$); we only adopt stars that have a measurement of both these values in K2-GAP. We determine asteroseismic masses and radii by combining these parameters with scaling relations via radius and mass coefficients ($\kappa_{\rm M}$ and $\kappa_{\rm R}$, respectively; Sharma et al. 2016):

$$\frac{R}{R_\odot} \approx \left(\frac{\nu_{\rm max}}{\nu_{\rm max,\odot}}\right)\left(\frac{\Delta\nu}{f_{\Delta\nu}\Delta\nu_\odot}\right)^{-2}\left(\frac{T_{\rm eff}}{T_{\rm eff,\odot}}\right)^{1/2} \equiv \kappa_R\left(\frac{T_{\rm eff}}{T_{\rm eff,\odot}}\right)^{1/2} \quad (1)$$

$$\frac{M}{M_\odot} \approx \left(\frac{\nu_{\rm max}}{\nu_{\rm max,\odot}}\right)^{3}\left(\frac{\Delta\nu}{f_{\Delta\nu}\Delta\nu_\odot}\right)^{-4}\left(\frac{T_{\rm eff}}{T_{\rm eff,\odot}}\right)^{3/2} \equiv \kappa_M\left(\frac{T_{\rm eff}}{T_{\rm eff,\odot}}\right)^{3/2} \quad (2)$$

As the scaling relations were originally calibrated to the Sun, extra calibrations (with the help of stellar models) were needed to make these relations appropriate for red giant stars, as frequency spacings are impacted by stellar structure (White et al. 2011), and therefore not simply related to mean density. In the above, $f_{\Delta\nu}$ represents a model-dependent correction to the observed $\Delta\nu$ values. Its value depends on, in part, the temperature and metallicity of the star. In K2-GAP DR3 (Z22), the EPIC served as the source for this temperature and metallicity. With APOGEE DR17 temperatures and metallicities in hand, we update $f_{\Delta\nu}$ using `Asfgrid` (Sharma et al. 2016) with its low-mass low-metallicity extension (Stello & Sharma 2022), in accordance with the treatment described in Z22, including alpha-dependent corrections to the metallicities. In the APOKASC publications, the so far published K2-GAP work, and in this work, our asteroseismic parameters adopt the method found in APOKASC-2, where we adopt an empirical calibration against fundamental data to set the $\nu_{\rm max}$ zero-point (see Z22 for more details). Our catalog includes masses and radii using $f_{\Delta\nu}$ and $\nu_{\rm max}$ values that have been updated since their initial calculation in Z22. For $\nu_{\rm max}$, the empirical evolutionary-state corrections from Z22 are removed and re-applied using the spectroscopic evolutionary states used here; the solar reference value, $\nu_{\rm max,\odot}$, for both red giant branch and red clump stars, is taken to be 3076μHz. $f_{\Delta\nu}$ values have similarly been recalculated with our new spectroscopic evolutionary states and updated APOGEE DR17 temperatures and metallicities. We include the updated $f_{\Delta\nu}$ and an associated flag to indicate quality of those values, mass and radii coefficients, stellar masses and radii, and their associated errors in Table 2.

We note that the K2-GAP DR3 asteroseismic data were calibrated using Gaia-based distances inferred from bulk stellar motions from Gaia DR2 (Gaia Collaboration et al. 2018) according to the methodology described in Schönrich et al. (2019) accounting for selection functions according to Schönrich & Aumer (2017). This technique corrects for bias in parallax, and indicates $\approx 10\mu as$ positional variations in the Gaia parallax zero-point across K2 campaigns. Gaia DR3 parallaxes corrected according to Gaia team recommendations (Lindegren et al. 2021) appear to still suffer from position-dependent parallax bias in K2 asteroseismic red giant samples (Khan et al. 2023), with a range in the bias of $\approx 40\mu as$ across K2 campaigns. A comparison of the K2-GAP DR3 asteroseismic radius scale to the Gaia DR3 radius scale computed according to Zinn et al. (2017) with parallax corrections from the Gaia team shows a 1.5% offset in the sense that the Gaia DR3 radii are smaller. Assuming this offset for a mass calibration via the $\nu_{\rm max}$ solar reference value (see Z22) would suggest a 4.5% downward revision of the asteroseismic masses. Such an offset is within the 2% systematic uncertainty in the $\nu_{\rm max}$ scale reported by Z22, and so while we note the possibility of a downward revision to the radius/mass scale here, we do not re-calibrate the asteroseismic data to Gaia DR3 parallaxes, particularly given indications of position-dependent Gaia DR3 parallax bias at a similar level.

2.3. *Spectroscopic Data*

Through detailed studies of the stars in the Milky Way, the Apache Point observatory Galactic Evolution Experiment (APOGEE, Majewski et al. 2017) is unravelling the compositional form of our Galaxy. APOGEE uses a high-resolution (R ∼ 22,500), infrared spectrograph (Wilson et al. 2019) operating in the H-band.

[2] https://kasoc.phys.au.dk

For the Northern Hemisphere observations, APOGEE is mounted on the Sloan Foundation 2.5m telescope (Gunn et al. 2006) at Apache Point Observatory, New Mexico. In the southern hemisphere the 40-inch Irénée DuPont telescope (Bowen & Vaughan 1973) at Las Campanas Observatory, Chile, houses the instrument.

APOGEE data are reduced, wavelength-calibrated, and co-added according to Nidever et al. (2015). Spectroscopic parameters are calculated using the APOGEE Stellar Parameters and Chemical Abundances Pipeline (ASPCAP; Holtzman et al. 2015; García Pérez et al. 2016) and calibrated according to Holtzman et al. (2018), with the model grids and the interpolation method described by Jönsson et al. (2020). APOGEE primarily targeted K2 evolved stars (RGB and RC) as they are intrinsically luminous with significant flux in the infrared; allowing high SNR observations at large distances. K2-GAP stars that were not already observed in the GALAH survey (Buder et al. 2021) were prioritized, although overlapping stars at lower priority were also observed. About half of the targets observed by APOGEE reside in the disk of the Milky Way ($b \leq 16°$), with the remaining targets split between the bulge and halo. Information on K2 object targeting can be found in Zasowski et al. (2017); Beaton et al. (2021) and Santana et al. (2021); the latter two papers include information on the relative weighting of the different classes of targets.

In this work, we use APOGEE data obtained during the fourth phase of the Sloan Digital Sky Survey (hereafter SDSS-IV) (Blanton et al. 2017) and analyzed in the seventeenth (and final) data release (Abdurro'uf et al. 2021) of SDSS-IV (hereafter DR17). DR17 contains 675,000 APOGEE targets over an additional two years of SDSS observations, in both hemispheres, compared to DR16 (Jönsson et al. 2020). The cumulative nature of SDSS data sets means that DR17 contains a reprocessing of all data obtained, processed, and released in previous data releases. Although many beneficial, and significant, updates appear in the DR17 release we only detail changes to the data release and reduction process relevant to this work. These changes primarily affect the abundances, because APOGEE uses the infrared flux method (IRFM) as an absolute standard for effective temperature, and asteroseismology for the absolute standard for $\log(g)$. For instance, ASCPAP was updated for DR17, with new sets of spectral synthesis grids including non–local thermodynamic equilibrium effects for Na, Mg, K, and Ca, which will be considered more in an upcoming APO-K2 abundance paper (Schonhut-Stasik et al., in prep.).

In the APOKASC samples (Pinsonneault et al. 2014, 2018), asteroseismic evolutionary states were employed to differentiate between the RGB and RC stars. For the purposes of this work, we adopt spectro-asteroseismic evolutionary states. These are calculated by a similar method as described in Warfield et al. (2021), and they depend on recalculating the temperature-, surface gravity-, and abundance-dependent cut performed in Warfield et al. (2021). Therefore, these spectroscopic evolutionary states rely on values of $T_{\rm eff}$, log (g), and elemental abundances from APOGEE DR17, and are trained on the asteroseismically-derived RGB and RC classifications from APOKASC3 (Pinsonneault et al., in prep). Ultimately, we assign stars as being on the RGB if their uncalibrated surface gravity[3] $\log{(g)}_{\rm SPEC} < 2.30$, or, where $\log{(g)}_{\rm SPEC} \geq 2.30$, if

$$[{\rm C/N}] \times 10^3 < 59.15 \; - \; 3.455 \; (155.1[{\rm Fe/H}]_{\rm SPEC} \; + \; \Delta T) \tag{3}$$

In this equation, $\Delta T = T_{\rm eff}^{\rm (SPEC)} - T_{\rm ref}$ is the difference between a star's uncalibrated effective temperature and its 'reference' temperature, calculated from a fit to the ridge-line of known RGB stars in the APOKASC3 dataset, which we define as

$$T_{\rm ref} = 4427.18 - 399.5[{\rm Fe/H}]_{\rm SPEC} + 553.17(\log{(g)} - 2.5) \tag{4}$$

Although these new evolutionary states show promise in that they are reliable in classifying the states accurately, there is a harder boundary in the $\log(g)$ space than we see when using asteroseismology-only derived evolutionary states. For example, there are few RC stars above a $\log(g)$ of 2.2 and this should be considered when dealing with stars in this domain.

2.4. *Astrometric Data*

The largest ever source of precise astrometric data comes from the *Gaia* mission (Gaia Collaboration et al. 2016), which was launched in 2013 and measured the six-dimensional spatial and velocity distribution of nearly two billion stars in the Milky Way. The astrometric information in this work comes from the the third data release of *Gaia* (hereafter *Gaia* DR3 or DR3; Gaia Collaboration et al. 2023) by selecting on 2MASS ID using the Gaia team–provided Gaia DR2–2MASS cross-match (Marrese et al. 2019) and Gaia DR2–Gaia DR3 ID cross-match (Torra et al. 2021).

3. RESULTS

[3] In the APOGEE catalog, the "SPEC" subscript marks the uncalibrated version of the parameter.

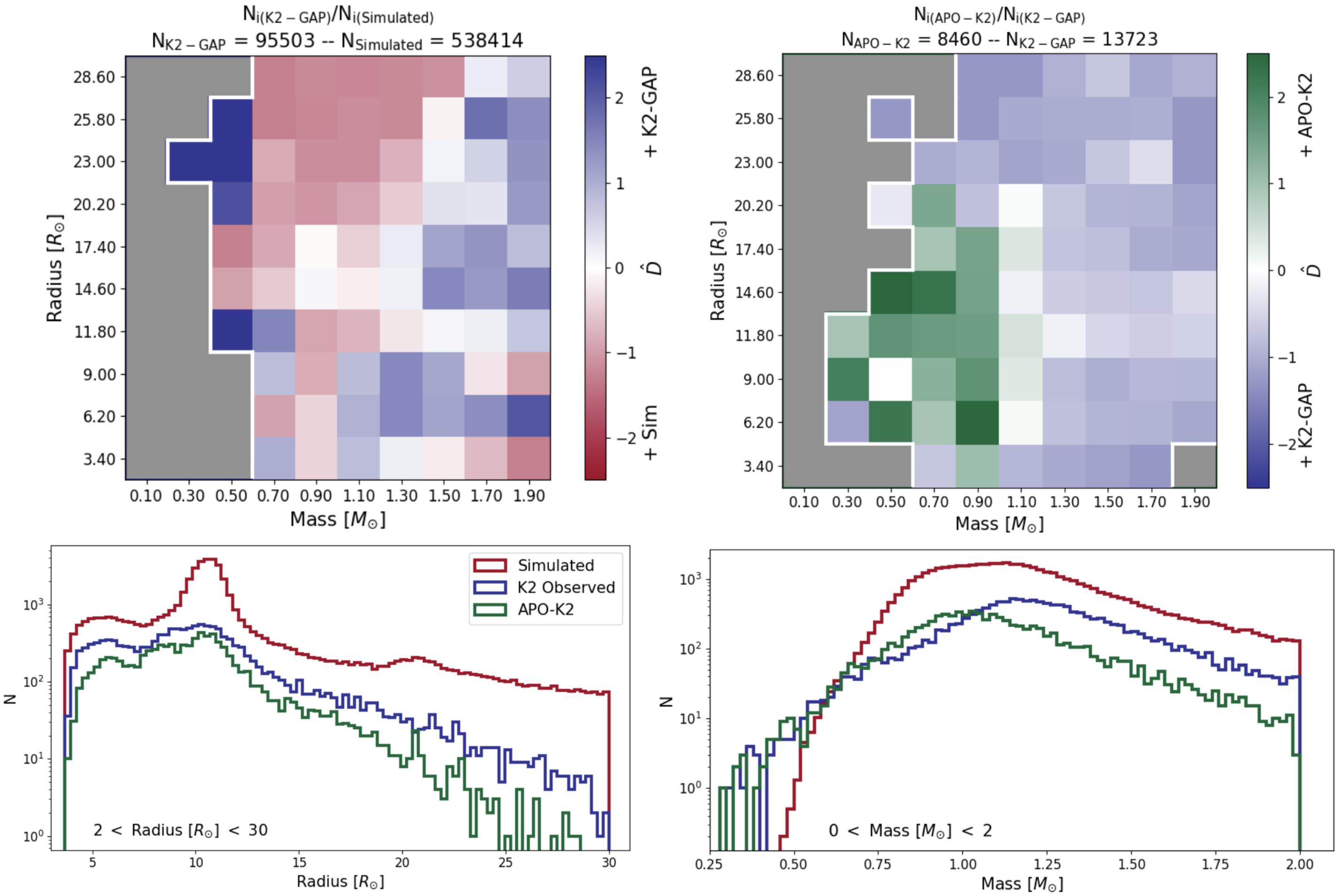

Figure 1. A collection of plots describing the completeness of our sample through an analysis of the selection function, by first comparing the simulated and K2-GAP samples, then the K2-GAP and APO-K2 samples. *Top Left:* A 10×10 grid showing the scaled fractional density of K2-GAP stars compared to the simulated sample in the mass [$M_\odot$] vs. radius [$R_\odot$] space. The title displays the number of stars in each of the samples overall; these values correspond to the scaling relation in the second term of Equation 7. The color-bar shows the varying scaled density in each bin from an over abundance of simulated stars in red to an over abundance of K2-GAP stars in blue, compared to expectations. Because $\hat{D}$ contains an asinh scale, the color-bar is centered around 0, which corresponds to an equal number of stars in both bins. The grey area, bordered in white, delineates between bins with real numbers allocated and those that are calculated to have 'nan' or 'inf' values, due to the bin being populated by no star in either the simulated or K2-GAP samples. *Top Right:* The same as the top left but for the density of APO-K2 stars over K2-GAP stars, with an abundance of APO-K2 stars shown in green and an abundance of K2-GAP stars, again shown in blue. *Bottom Left:* Three histograms showing the distribution in radius between $2 < R$ [$R_\odot$] < 30 of each sample (when cut on radius and mass); the simulated sample (red), the K2-GAP sample (blue), and the APO-K2 sample (green). In all plots, the simulated stars have been multiplied by a scaling factor of 0.1, to account for the over-sampling discussed in S22. *Bottom Right:* The same as the bottom left but showing the distribution of masses over $0 < M$ [$M_\odot$] < 2.

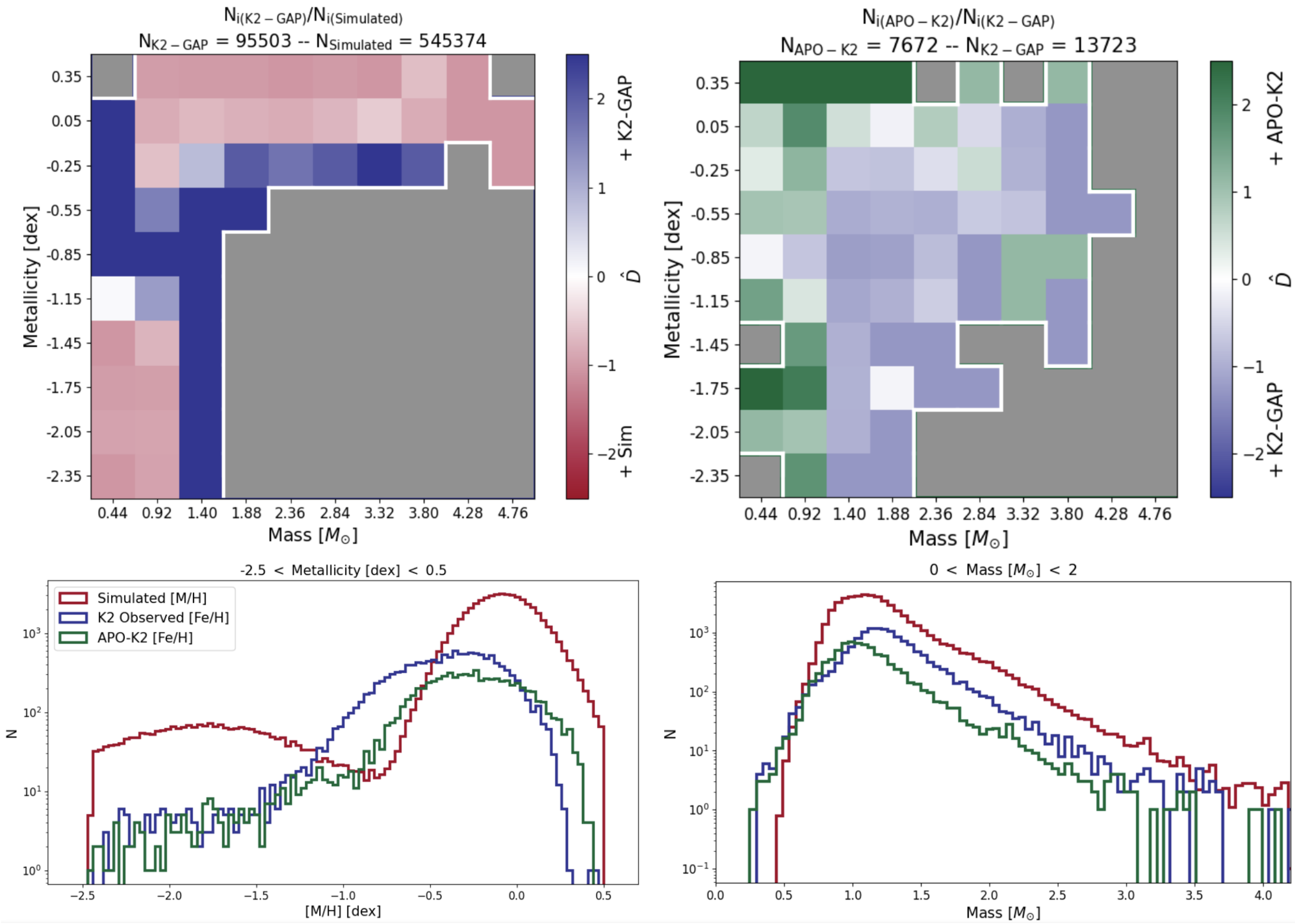

Figure 2. Same as Figure 1 but in mass [$M_\odot$] vs metallicity [dex] space. The scaling values can be determined from the plot titles. The metallicity histogram (bottom left) ranges from -2.5 < [M/H] [dex] < 0.5, and the mass histogram (bottom right) ranges from 0 < Mass [$M_\odot$] < 2. See Figure 1 for more general information.

In this section we begin by exploring the selection function (Section 3.1). We then detail the catalog provided in this work (Section 3.2). In Section 3.3 we discuss the overall metallicity as a function of campaign, before finishing with an exploration of the sample in terms of evolutionary states (Sections 3.4 and 3.5).

3.1. *Selection Function*

This section investigates the multiple layers of targeting and selection that lead to the APO-K2 sample, so that interested readers may consider completeness when using our catalog. The APO-K2 sample is fundamentally comprised of K2-GAP DR3, cross-matched with APOGEE DR17, which therefore includes selection and targeting choices made by both K2-GAP and APOGEE DR17. Because there are no stars lost in the cross-match between APOGEE DR17 and Gaia DR3, the Gaia aspect of the selection function is irrelevant. In what follows, we consider known aspects of both of these selection functions in turn.

Although the purpose here is to understand the completeness of the APO-K2 sample, we stop short of comparing it to a true, underlying Galactic stellar population; instead we compare it to a set of simulated stars that are drawn from a parent mock Galactic stellar population, as generated by the `Galaxia` code (Sharma et al. 2011). These simulated stars are drawn according to the K2-GAP selection function in color and magnitude, and then have an expected asteroseismic selection function applied to only keep stars with greater than 90% expected probability of having detectable asteroseismic signals (Sharma et al. 2022).

Some important assumptions are made in the creation of this simulated sample that could affect our inferences on the completeness of the APO-K2 catalog: for example, the assumed metallicity of the thin and thick disks (discussed further in our interpretation of Figure

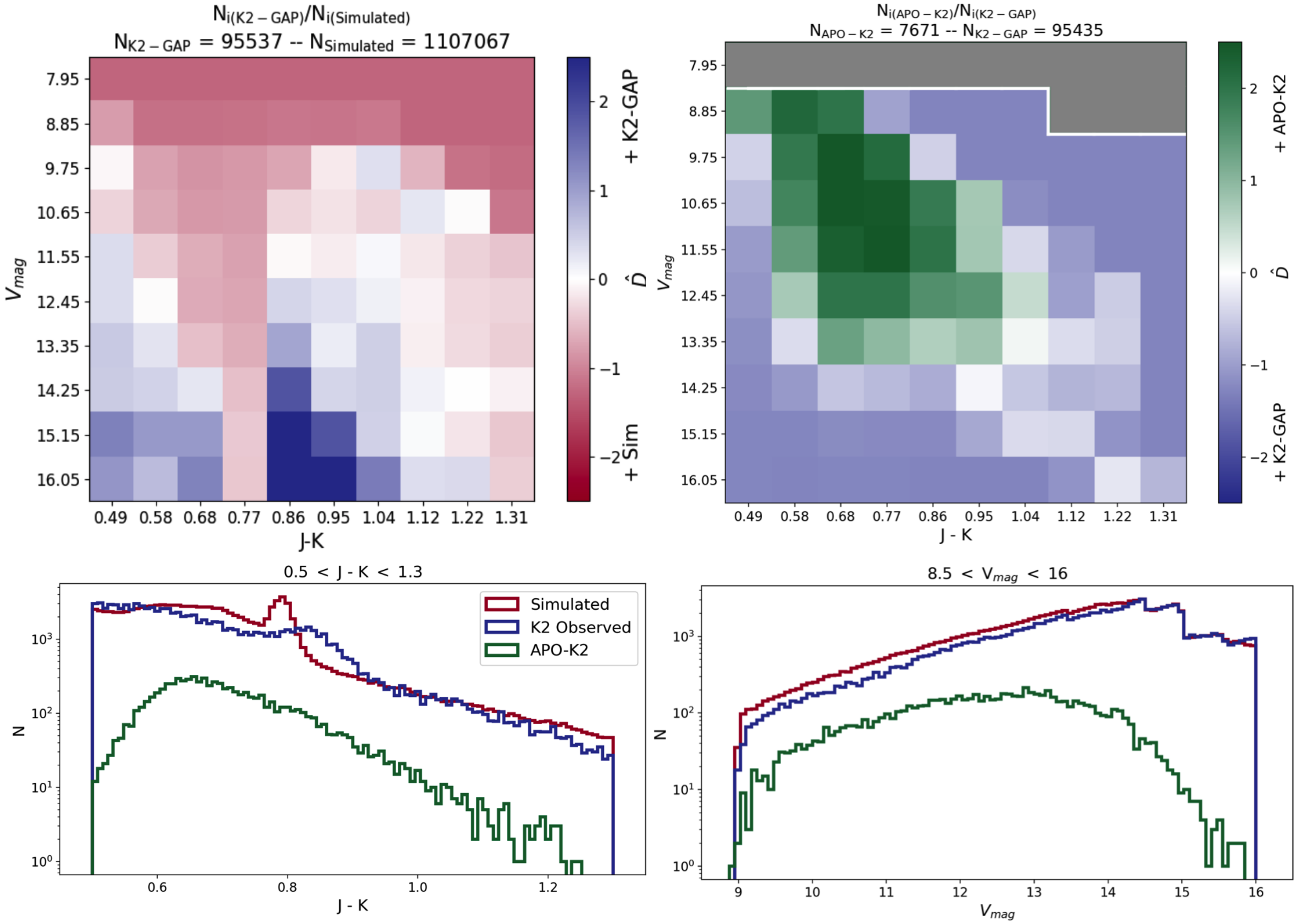

Figure 3. Same as Figure 1 but in color (J - K) vs magnitude (V_{mag}). Again, the scaling value can be determined from the plot titles. The color histogram (bottom left) ranges from 0.5 < J - K_s < 1.3, and the magnitude histogram (bottom right) ranges from 8.5 < V_{mag} < 16. See Figure 1 for more general information.

2) and the choices related to star formation history (which directly impact the distribution of κ_M, and as a consequence, mass).

3.1.1. *K2-GAP Selection*

The targets for the K2-GAP sample were chosen with a color cut. Broadly, the cut removed mostly dwarfs, with (J - K_s) < 0.5, corresponding to dwarfs with M_{Ks} > 1. This cut did exclude some giants, such as those on the horizontal branch (the blue extension of the RC); however, these are mostly rare, metal-poor stars, and are too hot to support solar-like oscillations.

For C1, C2, and C3, the 2MASS H-band magnitude was used to select in brightness. For later campaigns, an approximation of the V-band magnitude measured from 2MASS J and K_s bands was used, as per Eq. 5 below. This cut was chosen for later campaigns because K2 collects data in the K_p band, which is significantly

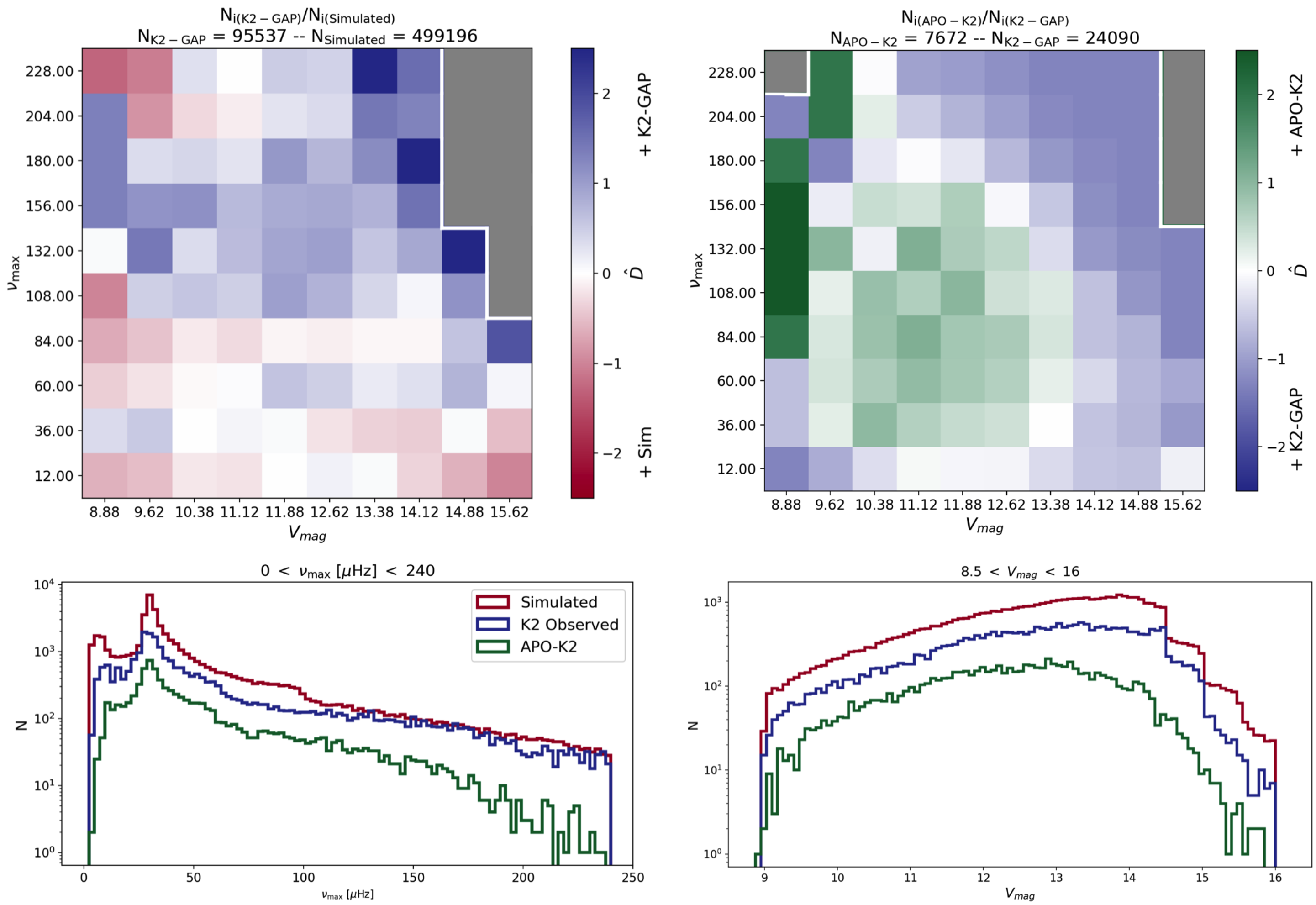

Figure 4. Same as Figure 1 but in magnitude (V_{mag}) vs ν_{max} [μHz]. The scaling values can be determined from the plot titles. The ν_{max} histogram (bottom left) ranges from $0 < \nu_{max}$ [μHz] < 240, and the magnitude histogram (bottom right) ranges from $8.5 < V_{mag} < 16$. See Figure 1 for more general information.

bluer than the H-band, and more consistent with the V-band (see Sharma et al. (2022) for more details):

$$V_{JK_s} = K_s + 2.0(J - K_s + 0.14) + 0.382 \exp\left[(J - K_s - 0.2)/0.50\right] \quad (5)$$

3.1.2. *APOGEE Selection*

By cross-matching with APOGEE we insert elements of the APOGEE selection function into our catalog. Beaton et al. (2021) discusses the prioritization scheme for the targeting in each field of the K2 program. This provides a meaningful comparison between targeted and observed stellar populations, and can be used to judge the completeness of our sample, in parameter spaces that may have been affected by our cross-match.

3.1.3. *Comparing Targeting and Selection Functions*

We compare our sample of APO-K2 stars to the K2-GAP stars and the simulated stars from S22[4]. We note that the values of asteroseismic mass and radius that we report are the average over a number of pipelines from Z22, whereas the K2-GAP data only use the SYD pipeline (Huber et al. 2009), which may cause a small difference in the inferred selection function when mapping from K2 data to APO-K2.

From here we investigate four parameter spaces: mass vs. radius (Figure 1), mass vs. metallicity (Figure 2), color vs. magnitude (Figure 3), and magnitude vs. ν_{max}

[4] github.com/sanjibs/k2gap and http://www.physics.usyd.edu.au/k2gap/ — using `data_name = 'Galaxia-K2-sydai2-mrtd5'` for the simulated stars stars, and `data_name = 'k2-sydai2'` for the K2 observed stars, being mindful to choose only stars within the campaigns we use in APO-K2 by selecting on '`cno`'.

(4). In each space, depending on the relative density being computed, we cut down the larger sample to match the limits of the smaller sample[5]. We created two 10 × 10 grids, in the investigated parameter space; for example, in the mass vs. radius regime we bin in a 10 × 10 grid of mass and radius. We populated these grids with the relative density of stars; one corresponding to the ratio of the observed K2 sample to the simulated sample, and one corresponding to the ratio of the observed K2 sample to the APO-K2 sample. This allows us to determine which stars are lost due to unknown aspects of the asteroseismic selection function (e.g., due to unexpectedly low signal-to-noise in the data compared to Sharma et al. (2022) simulations) and which are lost from the APO-K2 catalog due to the APOGEE selection function. When considering the simulated sample we multiplied the amount of stars in each bin by 0.1, to compensate for how the simulated stars were oversampled by a factor of 10 to reduce Poisson noise (see explanation in Sharma et al. (2022)). In all the density plots (the top row of Figures 1, 2, 3, and 4) grey areas cover bins where 'nan' or 'inf' values were calculated; this occurs when one of the samples has no stars in that bin. The resulting relative densities (D) were calculated and multiplied by a scaling factor (the second term in Equations 6 and 7) that is specific to the parameter space. These scalings allow the reader to plainly see the differences in the bins. These equations are shown below, for the density of the K2-GAP sample relative to the simulated sample:

$$\mathrm{D} = \frac{N_{i(\mathrm{K2-GAP})}}{N_{i(\mathrm{sim})}} \times \frac{N_{\mathrm{sim}}}{N_{\mathrm{K2-GAP}}} \tag{6}$$

and for the density of the APO-K2 sample relative to the K2-GAP sample,

$$\mathrm{D} = \frac{N_{i(\mathrm{APO-K2})}}{N_{i(\mathrm{K2-GAP})}} \times \frac{N_{\mathrm{K2-GAP}}}{N_{\mathrm{APO-K2}}}, \tag{7}$$

where the first term represents the relative density between the samples for that bin. Another scaling was applied to all bins, to more easily see structure in the selection function (Equation 8). Using the value of x = 0.6 (for the mass-radius space) and x = 1.0 (for the other parameter spaces) in the denominator will tend the scaling toward a log-scale at < -0.6 and > 0.6, and < -1.0 and > 1.0, respectively.

$$\hat{\mathrm{D}} = \mathrm{arcsinh}\left[\frac{D-1}{x}\right] \tag{8}$$

[5] For example, when calculating the number density between the K2-GAP and simulated sample, we cut the simulated data to match the K2-GAP data limits.

One of the key distributions, when considering Galactic archaeology, is mass. The mass distribution we would expect to see would be indicative of the star formation history and the lifetime of stars as a function of mass and metallicity (Wu et al. 2017). In terms of individual mass limits we expect a couple of clear boundaries. For example, no massive stars above 5 $\mathrm{M}_\odot$ because they would be too hot at the surface gravities probed by K2 to sustain solar-like oscillations. The lowest mass stars we expect would correspond to the age of the Galaxy, discussed further in Section 4.1. Higher or lower masses than these bounds likely reflect mergers, binary mass transfer, or mass loss.

Figure 1 shows density plots in mass $[M_\odot]$ vs. radius $[R_\odot]$ and histograms for these parameters. The color-bar on the density plot indicates the scaled fractional density of stars. The scaling factor described in the second term of Equation 6 for the left hand plot is (538414/95503) $\sim$ 5.6 (Number of K2-GAP stars/Number of simulated stars) and (13723/8460) $\sim$ 1.6 (Number of APO-K2 stars/Number of K2-GAP stars) on the right (Equation 7). In the top left density plot, for K2-GAP/simulated stars, we see few simulated stars in the low mass regime. This is likely due to the uncertainties on mass adopted by the simulation, as they correspond to the median uncertainties for the data (Sharma et al. 2011). We used the temperatures, κ_M values, a 3% uncertainty on temperature (in alignment with EPIC temperature), and SYD κ_M errors to compute the fractional error on mass for the simulated stars. Over the whole sample, the fractional mass error for the simulated stars is around 24%, but 51% when the sample is cut to M $< 1\mathrm{M}_\odot$ stars. Therefore, as the simulation adopts median uncertainties from the data, the simulation errors for mass are underestimated, likely causing the deficit in mass we see in the low-mass regime for the simulated sample; this is also seen at the low mass end of the mass histogram. One could argue that the abundance of low-mass stars seen in the sample, that are absent in the simulated data, may be the result of mass loss (including mass transfer and binary interaction that the simulation does not account for), as discussed in works that investigate inferred mass loss from asteroseismic data (Miglio et al. 2012, 2021; Tailo et al. 2022; Howell et al. 2022; Kallinger et al. 2018, and Roberts et al., (in prep.)), however due to the level of uncertainty in the simulated sample at low masses, we do not wish to draw this conclusion here.

Looking to the top right plot, of the relative APO-K2 stars/K2-GAP stars, we see more APO-K2 stars at lower masses and radii (this is represented by the green bump on the left of the plot). This may be the result of a combination of the different temperatures (APOGEE vs. EPIC) and asteroseismic scales (K2-GAP vs. SYD) being used to calculate the masses and radii in these samples. To investigate the extent to which temperatures are the cause, we calculate the mean raw APOGEE temperatures and mean EPIC temperatures (used for the K2-GAP sample). The resulting temperature difference corresponds to a difference of ∼6% in mass.

On the bottom left, in the radii histogram, we see a bump at $10R_{\odot}$ that does not appear in the observed samples. This likely represents clump stars, which are underrepresented in the data, as it can be difficult to detect oscillations in RC (Mosser et al. 2018) with their lower oscillation amplitudes (Yu et al. 2018). The extent of this bump in the histogram is due to the relatively long lifetime the stars spend in the clump relative to the RGB. RC stars share a similar core mass, which dictates their similar radii to one another (however they do not share the same envelope mass).

Figure 2 shows the density plots for mass [$M_{\odot}$] and metallicity [dex]. In this case, we used [M/H] values[6] for the simulated stars, and [Fe/H] for APO-K2 and the K2-GAP sample, as [Fe/H] was unavailable for the simulated sample[7]. For the relative density of the K2-GAP/simulated sample we see a bimodal distribution separated by an area where the relative amount of observed stars is higher. The bimodal distribution is ultimately due to the assumed metallicity of the thin and thick disks in the `Galaxia` model used to create the simulated stars, which we see in the distribution of the simulated sample's metallicities (a lower metallicity peak corresponding to the thick disk and a higher metallicity peak corresponding to the thin disk).

On the right hand side, showing the relative density of K2-GAP stars/APO-K2, we see more colored bins, indicating the presence of more populated bins. This demonstrates that although these stars were observed in K2-GAP they did not appear in the simulated sample, resulting in the grey area on the left hand density plot.

In the mass histogram, again we see an wealth of lower mass stars ($\approx 0.6 - 1\ M_{\odot}$) in the APO-K2 sample, and that more stars were observed at lower masses in K2 than found in the simulated sample. Note the difference in mass range for the density plots in Figure 1 compared to Figure 2. The mass range in Figure 1 is purposefully more condensed to show the detail toward smaller masses.

In Figure 3, we show the color-magnitude space. These plots clearly show color cuts enforced by the K2-GAP target selection, where C1 and C2 have a maximum magnitude of 7 in H-band, and all other campaigns have a maximum magnitude of $V_{\rm JK} = 9$ (see Table 1 of S22). This is evident both in the histograms, and in the top left density plot that shows many more simulated bight stars at the top of the plot. In the right hand histogram we see very good agreement between the simulated stars and the observed K2-GAP stars. This is due to the selection function for targeting taking place in V-band, and these cuts being easily replicated in the simulation. In the top left density plot for the K2-GAP/simulated sample we see an abundance of simulated stars in the column of bins corresponding to ∼0.77 in J-K. This corresponds to the peak in the bottom left histogram, representing the RC stars. We note that the `Galaxia` simulation does not include extinction, so the blue edge may be due to the cut off in J-K_s observation: the simulated sample is not seeing some stars that would be reddened and pass the J-K_s cut. This lack of extinction is also evident in the histograms, which show the red clump stars appearing redder and more smeared out in the K2-GAP color histogram compared to the cleaner peak in the simulated sample. Finally, the simulations assume a color dependence to the amplitude of oscillation, which may cause a mis-match between the assumed and actual color distributions.

Figure 4 shows the $\nu_{\rm max}$ vs. magnitude space. S22 plot their selection function in this same parameter space (bottom right hand plot of Figure 10 in S22), and the top left density plot in this figure shows similar results, confirming consistency in our work. We see more faint, high-$\nu_{\rm max}$ K2-GAP stars, and in the density plot on the right, we see a shift in the distribution, imposed by the APOGEE selection. In the upper right corner of this plot, we see fewer APO-K2 stars, corresponding to fewer of the seismically low SNR stars. The histograms also show an overabundance of stars at lower $\nu_{\rm max}$ values corresponding to stars that are difficult to measure due to there being few modes for low $\nu_{\rm max}$, which sit at the limit of the resolution of the K2-GAP light curves (Z22). The histograms between the K2-GAP stars and the simulated stars match well in $\nu_{\rm max}$ and magnitude space because the selection of stars for the K2-GAP sample were based on the ability to determine pulsations, and the simulated sample were selection-function-matched to the catalog (provided in S22) and designed to determine the completeness of the K2-GAP observed stars.

[6] When discussing abundances in this work we use the standard notation: $[{\rm X/Fe}] \equiv \log_{10}\left(\frac{\rm X}{\rm Fe}\right) - \log_{10}\left(\frac{\rm X_{\odot}}{\rm Fe_{\odot}}\right)$.

[7] [M/H] is the average bulk metallicity in APOGEE, while [Fe/H] involves a selected subset of iron lines. In practice, the two agree closely for most APOGEE stars, since optical metallicity values track iron abundances (See https://www.sdss3.org/dr10/irspec/aspcap.php for more information.)

The selection function plots for individual campaigns can be found on the companion GitHub. It is important to consider the selection function over each campaign due to potential differences (discussed in S22), such as light curve duration, pointing accuracy, and the variation in crowding. For those interested in studying completeness in the sample, both in individual campaigns and as a whole, the GitHub also includes tabulated values of the density plots with files for the bin edges, and for the fractional densities of K2-GAP/simulated and APO-K2/K2.

3.2. *The APO-K2 Catalog*

The public catalog distributed with this publication contains a row for each star. In this paper the catalog is broken down into four distinct tables. Table 1 includes EPIC, APOGEE, and Gaia DR3 ID numbers, the K2 campaign number, coordinates in RA and Dec as well as Galactic coordinates, spectro-asteroseismic evolutionary states[8], and the calibrated $T_{\rm eff}$ and $\log(g)$ from APOGEE, with their associated errors.

Table 2 contains the asteroseismic parameters for the stars including $\nu_{\rm max}$, $\Delta\nu$, and $f_{\Delta\nu}$, mass, radius, and the corresponding mass and radius coefficients, all with their respective errors. There is also a flag that pertains to $f_{\Delta\nu}$, where an integer value of 0 indicates no issue with the calculation, an integer value of 1 indicates that $f_{\Delta\nu}$ is computed by extrapolating beyond the bounds of the $f_{\Delta\nu}$ grid, and an integer value of 2 indicates that $f_{\Delta\nu}$ could not be computed due to a lack of $\Delta\nu$.

Table 3 contains and elemental abundance information from APOGEE and magnitude and color information from the EPIC. The abundance information given is the [M/H], [Fe/H], and [α/M], each with their associated errors from APOGEE. There is also a flag indicating whether a source is high-[α/M] (1) or low-[α/M] (0), with an extra condition for stars that are close (within 2-σ) of the dividing line and/or have [Fe/H] < -1 (-1). Magnitude information includes the $V_{\rm JK}$ magnitude, calculated using the J- and $K_{\rm s}$-band magnitudes (also included), the J-$K_{\rm s}$ color and the associated errors for each, with the $V_{\rm JK}$ error calculated using the standard propagation of uncertainty.

The final Table (Table 4) contains kinematic and orbital information for the stars. The corrected parallax and error from *Gaia* DR3 are given and then the following parameters computed with the `Gala` module (Price-Whelan 2017; Price-Whelan et al. 2022) (and others, see Section 4.3): Galactic eccentricity, $|Z_{\rm max}|$ (the farthest point from the Galactic plane reached by the star in its orbit), angular momentum, total energy, and the U, V, and W components of the velocity. Each parameter also contains an associated error. The final flag provided is the DR3 flag which is nonzero if either of the following are true: the star is flagged in the `non_single_star` column of DR3, or the `fidelity_v2` value from Rybizki et al. (2022) is ≤ 0.5 or unavailable.

Access to the APO-K2 catalog can be found as an electronic table with this paper and on the companion GitHub (https://github.com/Jesstella/APO-K2). A frozen version of the data in this table can be found at Zenodo using the following DOI: https://doi.org/10.5281/zenodo.8373233. The public catalog contains all information needed to re-create the plots in this paper. The GitHub and paper website (https://www.jessicastasik.com/apo-k2) also contain supplemental plots, including the selection function density plots for the individual K2 campaigns, and their density matrices as .csv files. Furthermore, in the interest of accessibility, alternative text[9] for plots can also be found at these sources, as well as author information, and relevant conference presentations. The APOKASC-2 data used in this paper can be found directly at http://vizier.u-strasbg.fr/viz-bin/VizieR-3?-source=J/ApJS/215/19, or by way of Pinsonneault et al. (2018).

3.3. *Sample Metallicity*

K2 samples multiple Galactic lines of sight providing a broad overview of the metallicity distribution of the Milky Way. Overall, our catalog provides a range of metallicities for evolved stars, particularly in campaigns of high and low Galactic latitudes.

Figure 5 shows the [M/H] distribution for each K2 campaign. Each histogram contains all stars observed in the campaign, including those that appear in multiple campaigns. The bottom right histogram shows the metallicity distribution for the APOKASC-2 sample. C10 boasts the lowest mean metallicity with $\langle[\mathrm{M/H}]\rangle = -0.50$ [dex] at $b = 59.6°$[10]. The highest average metallicity is in C11 ($\langle[\mathrm{M/H}]\rangle = -0.05$ [dex] at $b = 9.1°$). This is in contrast to the APOKASC-2 histogram with a mean metallicity of -0.02 [dex] (at $b = 13.5°$); all of the K2 histograms have lower mean metallicity than the *Kepler* field.

Kepler's objective of observing nearby, solar-metallicity dwarf stars likely contributed to it observing relatively few metal-poor stars. In contrast, the

[8] Asteroseismic evolutionary states for the K2-GAP sample can be found in Zinn et al. (2022)

[9] For those who may be blind or visually impaired.

[10] Where b is the average Galactic latitude for the field.

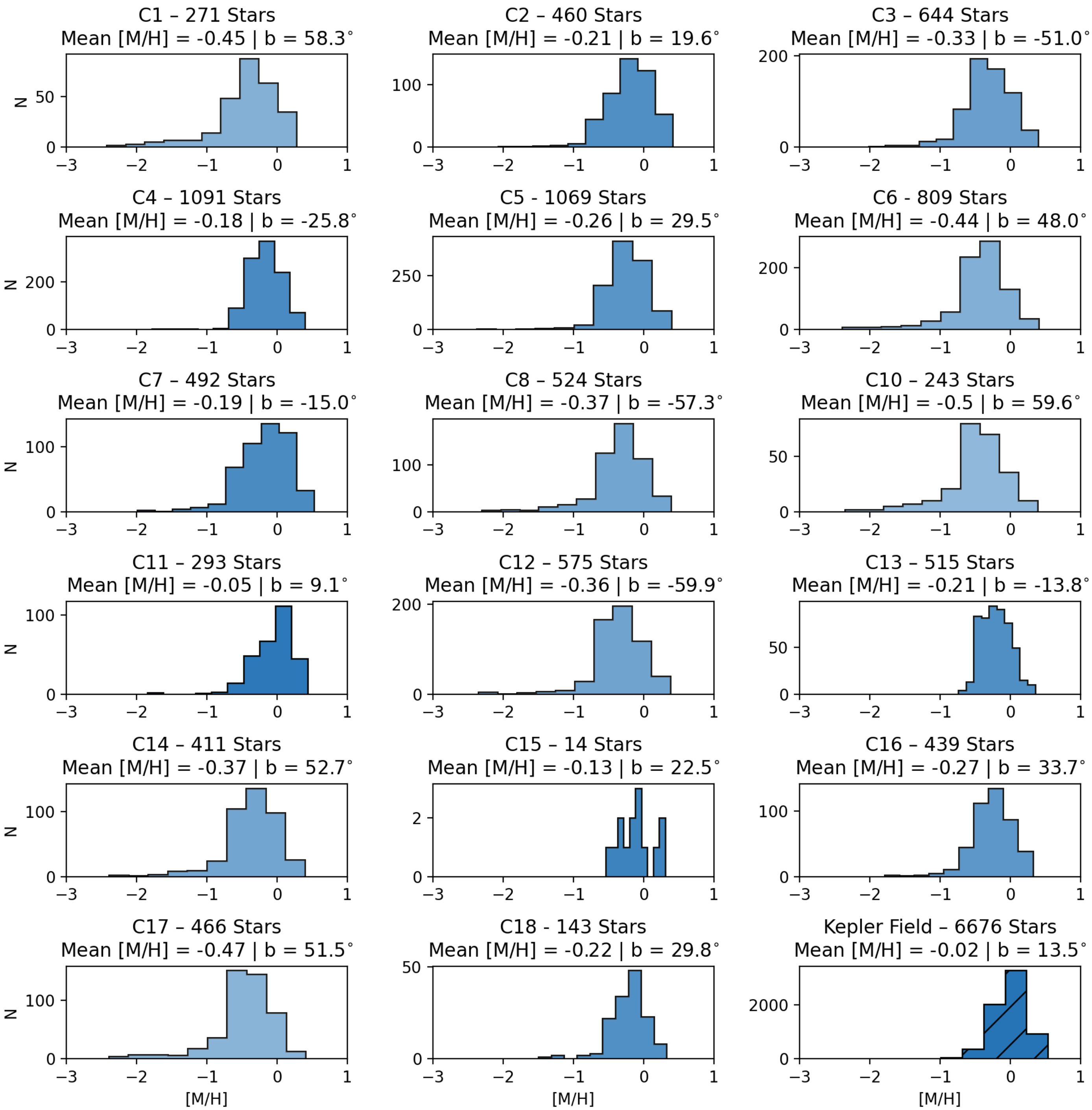

Figure 5. Each histogram shows the APOGEE [M/H] distribution for the K2 campaigns. The bottom right-hand plot, with hatched markings, is the metallicity distribution of the *Kepler* field taken from APOKASC-2. Color indicates the mean metallicity, with a darker blue corresponding to a higher mean metallicity. The title of each plot gives the campaign number, the number of stars in the campaign, the average metallicity, and the average Galactic latitude of the campaign field.

K2-GAP sample was selected with completeness of the evolved stars in mind, a sample ideal for Galactic archaeology. Apart from the observing selection function, the field choice itself is a determinative factor in the resulting metallicity distributions of *Kepler* v. K2: the K2 sample is, on average, farther away from the Galactic plane than the stars in the *Kepler* field. This is evident in Figures 5 and 6, as the stars at higher and lower Galactic latitude are generally more metal-poor.

3.4. *Sample Overview*

Our final APO-K2 sample contains 7,672 unique stars with spectroscopic, asteroseismic, and astrometric data. The sample includes a total of 8,460 observations, occurring across multiple campaigns, sometimes observing the same star in multiple campaigns. When separated into evolutionary states, we have 2,465 unique RC stars and 5,207 unique RGB stars. The extensive overlap (See Section 2.1) between the APOGEE catalog and K2-GAP program is due to the priority ordering for target selection (See Table 3 of S22). Targets were chosen for observation in K2-GAP according to criteria such as 2MASS and SDSS color and membership in existing spectroscopic survey catalogues, with each criterion given a priority ranking. This selection method gave the highest priority to APOGEE targets; APOGEE, in turn, prioritized observing spectra of K2-GAP stars resulting in the large overlap we see.

The sample reaches $\sim 60°$ above and below the plane of the Milky Way, and explores the Galactic Center. The position of these stars relative to the plane of the Milky Way are shown in Figure 6. Color represents [Fe/H] for each star in our sample (from APOGEE), with the color-bar scaled between -1.0 and 0.5 [dex]; the actual maximum and minimum values of [Fe/H] are -2.45 and 0.51 [dex], respectively. This scaling shows the relatively metal-rich state of the *Kepler* field in comparison to K2 and the metal-rich state of C2, C7, C11, and C15 relative to the other Campaigns; we discussed campaign-specific metallicities in Section 3.3. We do not include C9, nor C19 (see Section 2.2). Throughout this work we investigate, in particular, the low-metallicity stars specifically those below -1.0 [dex], which have not been available in large asteroseismic catalogs until now. For comparison, there are ~ 288 stars in this catalog with $[Fe/H] \leq -1.0$, and only ~ 35 in the APOKASC-2 catalog.

3.5. *Identifying Stellar Sub-Populations*

We separated the APO-K2 sample into two subsamples (RGB and RC) using their evolutionary states (as described in Section 2.3). Figure 7 illustrates that combining asteroseismology and spectroscopy enables us to decipher areas on the H-R diagram containing interesting details like the RGB bump and secondary red clump stars (Tayar et al. 2019). Figure 7 represents the stars on a H-R diagram. The left plot presents the RC stars prominently, with the RGB stars indicated by grey crosses in the background, and the right-hand side presents the RGB stars prominently, with the RC stars indicated by the grey crosses. By separating these two groups of stars, we hope to make the different samples clear to the reader. Figure 8 displays the same stars as in Figure 7 but in $\log(g) - T_{eff}$ space, also known as a Kiel diagram. The size of the points indicates the asteroseismically derived mass for Figure 7 and the left hand plot of Figure 8. The right hand side of Figure 8 has asteroseismically derived radius represented by point size.

These figures show a rich array of features that are qualitatively in agreement with the physics of RGB and RC phases of stellar evolution (Cox & Giuli 1968; Kippenhahn et al. 2013; Girardi 2016). We mention some of these patterns here, and ongoing investigation explores to what extent the RC observations are consistent with models as a function of mass and metallicity. These plots indicate the importance of precisely derived evolutionary states (see Section 2.3); there is **substantial** overlap between RGB stars and RC stars.

The combination of spectroscopic temperatures with well constrained asteroseismic radii (used to calculate luminosity) allows us to investigate small sub-samples of secondary RGB and RC bump stars. The RGB bump stars are clearly shown by an over density of grey crosses on the left-hand side of Figure 7, at a temperature of $\sim$4650K and $30L_{\odot}$.

When considering these plots as one sample, the RC stars are generally at higher temperatures than their RGB counterparts. The RC stars show an increase in mass with temperature and luminosity. Using mass as a proxy for age, this gradient implies youth at higher temperature and luminosity. A clear metallicity gradient can be seen with temperature, with lower metallicities corresponding to hotter stars. The existence of the secondary red clump is seen on the left-hand side of Figure 8, with a collection of stars around $\log(g) \sim 2.75$ dex and $T_{\rm eff} \sim 5000$ K. We explore possible secondary red clump stars further in Figure 9, as they are not seen clearly in the left hand plot of Figure 7.

The RGB stars also show a gradient in metallicity towards higher temperature and luminosity, most clearly in Figure 8, where metallicity decreases toward the left of the branch. This gradient also corresponds to increased radii (see marker size in Figure 8). These relationships and the slight dispersion of points at higher luminosities (representing a wider range of temperatures

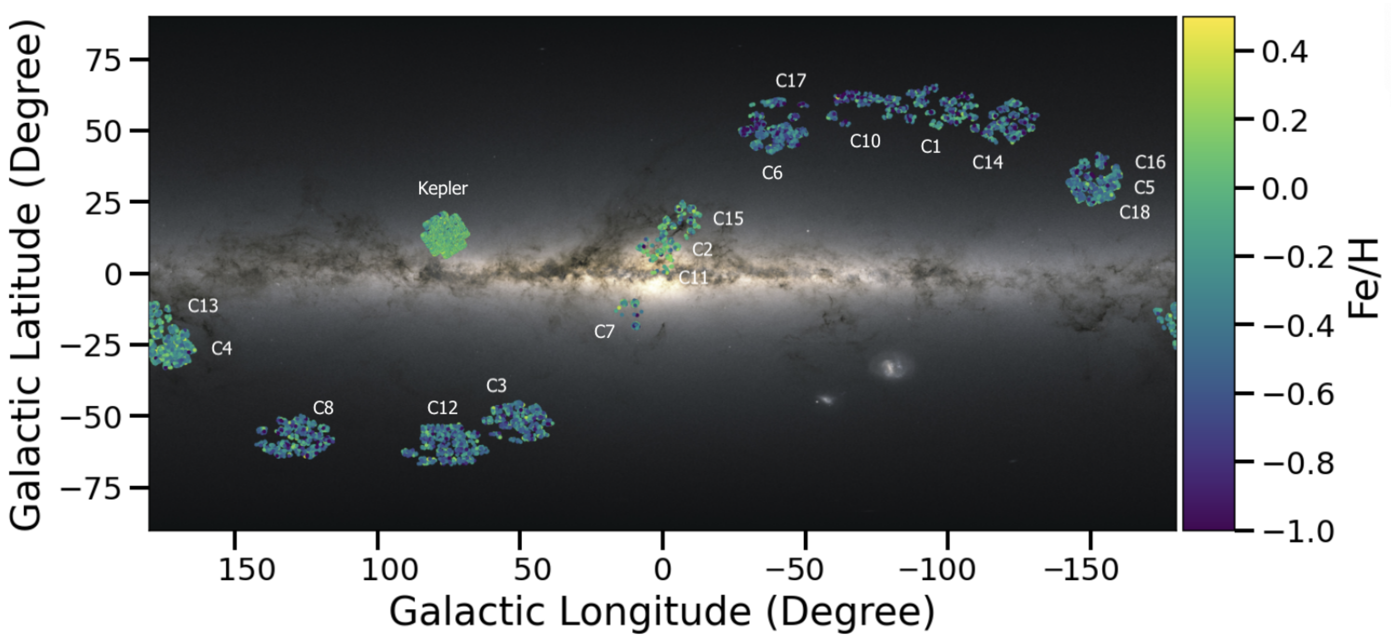

Figure 6. Footprint of each of the K2 campaigns in this sample, on a backdrop of the Milky Way, with axes representing the coordinates [degrees]. Each point represents a star in our catalog and color indicates its metallicity. The position of the *Kepler* mission field is shown for reference, also colored by metallicity [Fe/H], as taken from APOKASC-2. Gaps seen in the telescope's field of view correspond to CCD modules 3 and 7, which failed prior to the K2 mission. Each campaign is labelled with the campaign number in the format 'C[number]'. The metallicity color-bar has been scaled between -1.0 and 0.5 to show the resulting metallicity distribution within each campaign. C9 and C19 are not used and therefore not shown. Background image modified from ESA/Gaia/DPAC, and is applied using the `mw_plot` Python module and the `MWSkyProjection` map 'equirectangular.'

for the more luminous stars) may be representative of AGB stars, although it is difficult to fully determine stars belonging to the AGB. Using MIST models (Dotter 2016; Choi et al. 2016) we were able to rule out AGB stars at $\log(g) > 2.0$ with reasonable certainty, for low metallicity stars ([Fe/H] < -1.5), and with relative confidence at solar metallicities. However, we found a $\log(g)$ cut alone does not rule out all AGB stars.

Using this sample we attempt to make a distinction between secondary RC stars in different stages of evolution. In Figure 9 we further investigate possible members of the secondary red clump, outlined by eye in the pink box on the left hand plot of Figure 8. This plot shows RC stars plotted using four different parameters as a function of temperature. Each of these plots uses grey circles to show the RC sample as a whole, purple triangles to indicate stars with a luminosity $> 100\mathrm{L}_{\odot}$, and green diamonds to indicate stars with a mass $> 1.8\mathrm{M}_{\odot}$ and a luminosity $< 100\mathrm{L}_{\odot}$. The $1.8\mathrm{M}_{\odot}$ cut was used to select for secondary clump stars, which do not undergo a helium flash and therefore show a range of luminosities due to their range of core masses (Girardi 2016). In $\mathrm{T}_{\mathrm{eff}}$ vs. luminosity we see a number of high luminosity stars above the RC, whilst the the massive stars are hidden within the RC. We see in the mass vs. temperature space that the luminous stars are generally at least as massive as the less luminous high-mass stars. The high luminosity clump stars are therefore likely secondary red clump stars due to their high mass, but may be later in their evolution compared to the other high-mass clump stars. Indeed, we would expect their radii to expand with evolution as the core of the star contracts and heats up, consistent with the majority of them having radii $> 12.5\ \mathrm{R}_{\odot}$ and lower surface gravities. Still some of the luminous stars have masses larger than $2.5M_{\odot}$, and so would be expected to begin their red clump phase with luminosities that are already larger than less massive secondary clump stars at the beginning of their red clump phase (Girardi 2016).

To test whether the calculated uncertainties in mass and radius may be scattering the high luminosity stars above the high mass stars we calculated their mean errors in mass and radius. For the high luminosity stars, their mean error in mass is $0.46\ \mathrm{M}_{\odot}$ and their mean error in radius is $1.07\ \mathrm{R}_{\odot}$. For the high mass stars these values are $0.25\ \mathrm{M}_{\odot}$ and $0.43\ \mathrm{R}_{\odot}$, respectively. Although the mean error in radius for the high luminosity (purple) stars is roughly double that of the high mass stars (green) it is unlikely to account for the entire difference that we see between these groups, given that the mean radius for the high luminosity stars is $16.9\ \mathrm{R}_{\odot}$ and the mean radius for the high mass stars is $10.8\ \mathrm{R}_{\odot}$.

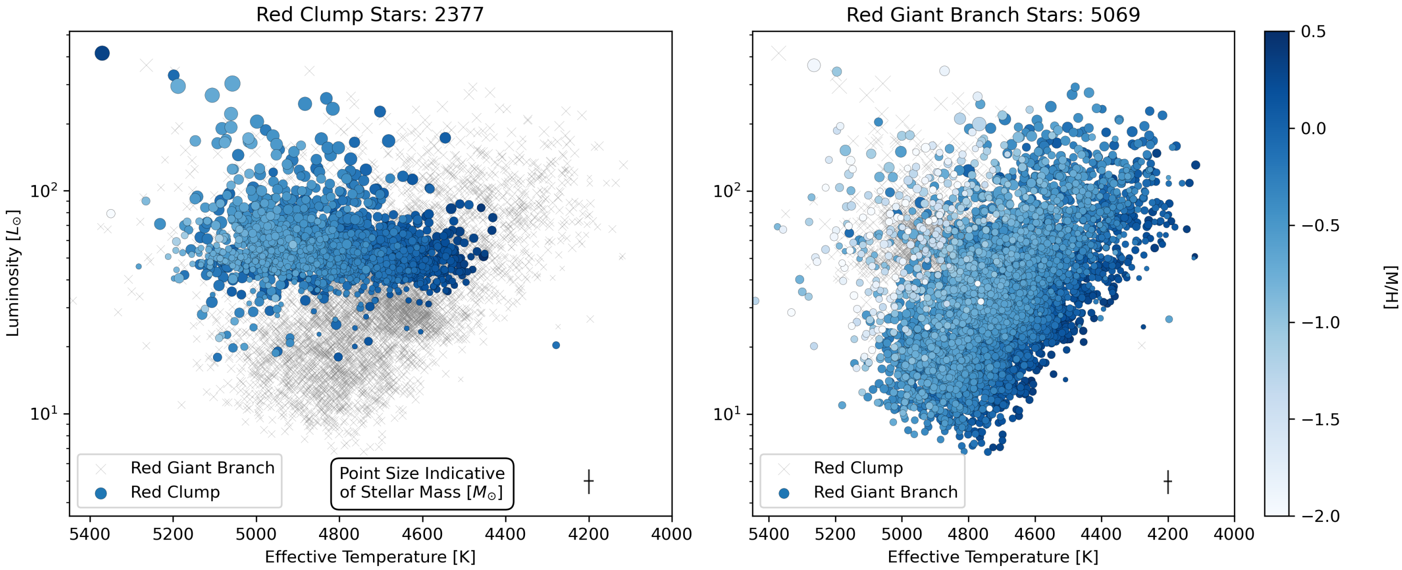

Figure 7. Two H-R diagrams showing the APO-K2 sample. *Left:* RC stars. *Right:* RGB stars. The title of each plot includes the number of stars in the plot. Only one observation of each star is plotted for stars that were observed in multiple campaigns. Stars with R $> 30R_\odot$ are removed. The marker size, for filled circles, corresponds to the asteroseismic stellar mass [$M_\odot$] (See Section 2.2) and the color scale corresponds to [M/H] [dex] from APOGEE, and has been scaled between -2.0 < [M/H] < 0.5 to show any relation in metallicity. A representative error bar is given in the lower right of each plot for the stars shown as filled circles. The points are ordered by metallicity in descending order so that low metallicity stars are plotted on the top of the scatter. Luminosity is calculated using the asteroseismic radius and APOGEE temperature.

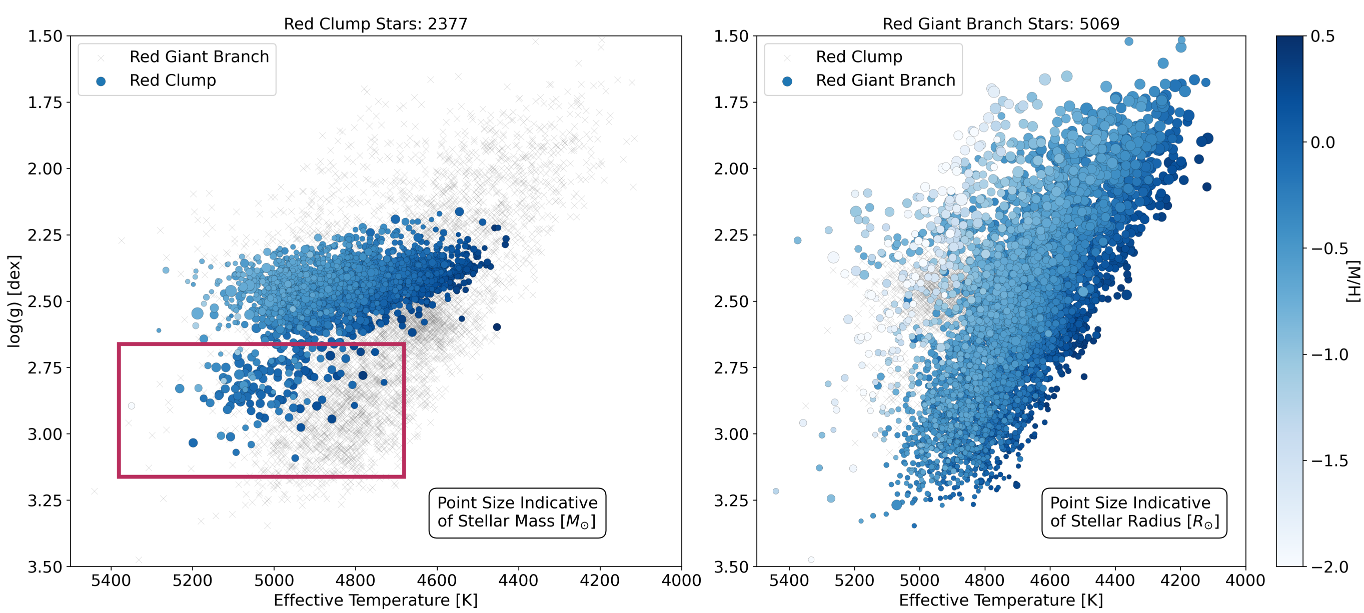

Figure 8. Two Kiel diagrams showing the APO-K2 sample. All cuts, color, and placement are the same as in Figure 7 with the exception of the circle size for the RGB plot (right), which is indicative of asteroseismic stellar radius, as opposed to stellar mass. The pink box outlines stars falling under the red clump, in the secondary red clump, and are explored in more detail in Figure 9.

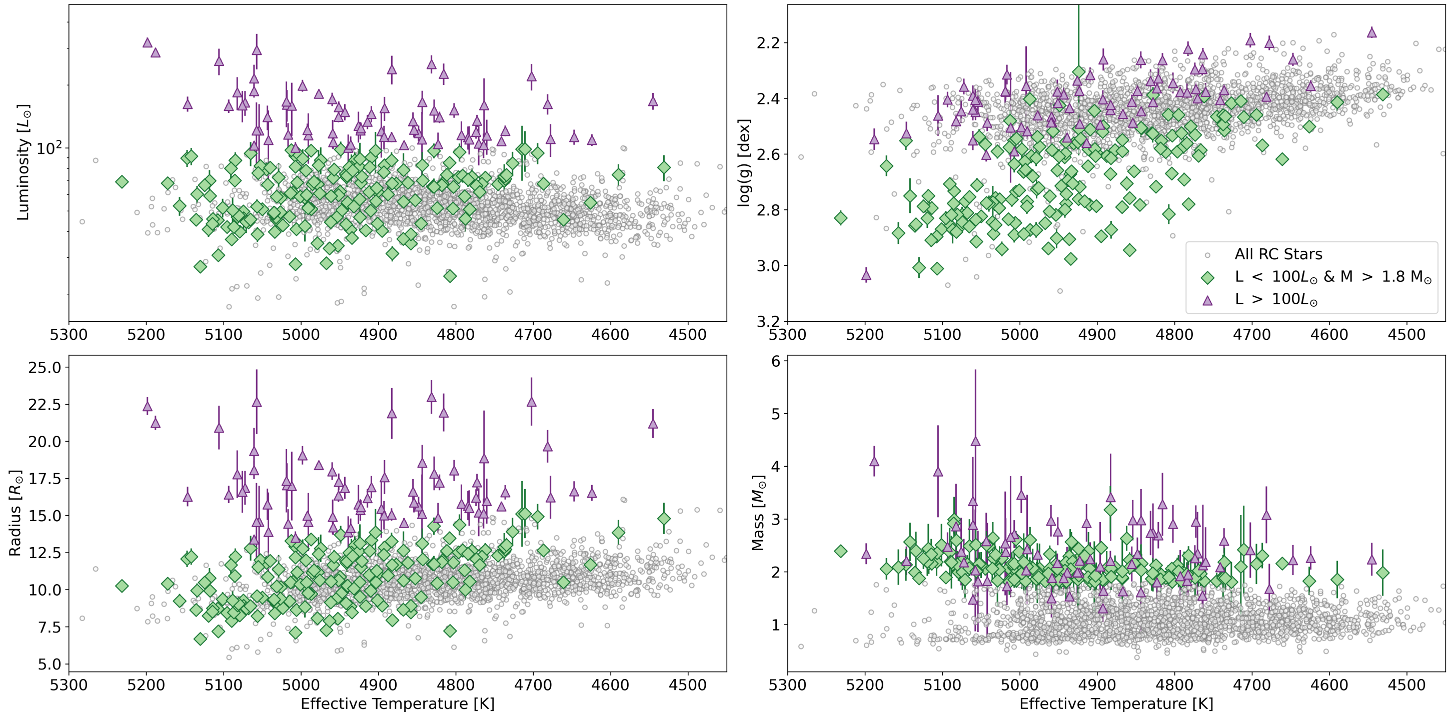

Figure 9. Four scatter plots showing the RC stars, in various parameter spaces. Each plot has $T_{\rm eff}$ on the x-axis and the y-axis depicting stellar Luminosity [$L_\odot$] (top left), log(g) [dex] (top right), Radius [$R_\odot$] (bottom left), and Mass [$M_\odot$] (bottom right), with their associated errors. The entire sample of RC stars is shown by grey circles. Stars with L > 100$L_\odot$ are represented by purple triangles and stars with L < 100$L_\odot$ and M > 1.8$M_\odot$ are shown by green diamonds.

3.6. *Comparison to APOKASC-2*

Pinsonneault et al. (2014) presented the initial combination of asteroseismic (*Kepler*) and spectroscopic (APOGEE) data for 1,916 evolved stars in the first APOKASC catalog (hereafter, APOKASC). They used the asteroseismic data to calibrate the relationships between parameters such as mass and age with spectroscopic observables. The second APOKASC release (Pinsonneault et al. 2018, hereafter APOKASC-2) looked at an additional 4,760 evolved stars (6,676 in total) with an empirical approach, combining asteroseismic measurements across different methodologies to calculate averaged values and reduce systematic errors. APOKASC used SDSS DR10 (Mészáros et al. 2013) parameters, and the APOKASC-2 used SDSS DR14 (Holtzman et al. 2015).

The K2-GAP asteroseismic parameters used here follow a similar averaging approach (Zinn et al. 2022) to APOKASC-2. The main difference between the approachs is in target selection. The K2 stars were chosen as a function of magnitude and color with the intention of creating a clean and easy to reproduce sample, unlike the *Kepler* stars. Indeed, Wolniewicz et al. (2021) found a strong selection bias against cool, low-luminosity, red giant stars in *Kepler*, where the observed red giants decrease from ≈ 80% at $K_{\rm p}$ = 14 mag to ≈ 50% at $K_{\rm p}$ = 15 mag; with only 40% of red giants at $K_{\rm p}$ = 15 being observed for more than 8 quarters. They note that the scarcity of observed red giants could be because the goal of *Kepler* was to observe solar-type stars; therefore, many identified red giants were removed from the target list after one quarter.

K2 is better suited to Galactic archaeology as compared to *Kepler* not just because of its well-understood and largely complete giant selection function. Due to its multiple Galactic lines of sight, it allows wider coverage of the Galaxy, observing multiple stellar populations at greater distances both radially and above and below the Galactic plane, thus broadening our understanding of the Galaxy's stellar composition as a whole. However, the downside to K2's wide coverage is the shorter length of lightcurves in comparison to *Kepler*, resulting in lower SNR, meaning that oscillation spectra are harder to analyze.

APO-K2 and APOKASC-2 also differ to APOKASC in the addition of stars in the low-metallicity regime (See Figure 5). These broader parameter spaces subsequently extend our understanding of related parameters, i.e. the low-mass/low-metallicity space (See Section 4.1) and the [α/Fe]-bimodality (See Section 4.2).

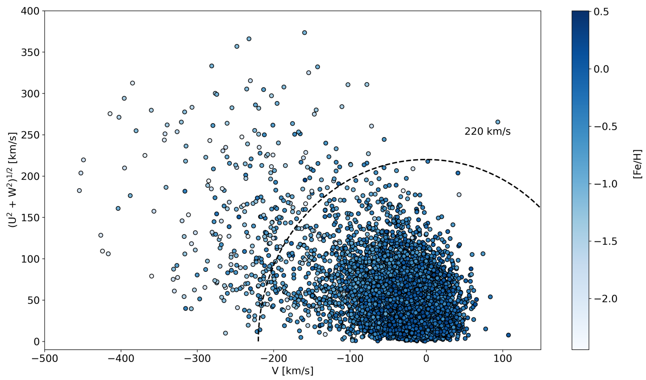

Figure 10. A Toomre diagram of our sample, showing stellar velocity relative to the local standard of rest. The colorbar in this plot represents [Fe/H] from APOGEE and a dotted black line represents a velocity of 220 [km/s]. This line is used to delineate between halo stars and the rest of the sample, for use in Figure 11. .

4. DISCUSSION: EXAMPLE APPLICATIONS OF THE APO-K2 CATALOG

4.1. *Asteroseismic Mass vs. Metallicity*

Epstein et al. (2014) showed that the asteroseismic masses determined through scaling relations in a handful of halo and thick disc APOKASC red giant stars were too large, under the assumption that such stars should be old and therefore of low mass. Sharma et al. (2016) subsequently re-analyzed these stars using a different temperature scale and $\nu_{\rm max}$ scale, which largely removed the discrepancy reported by Epstein et al. (2014). Following these observational findings, a theoretical motivation then emerged for a metallicity-dependent error in asteroseismic masses due to the $\nu_{\rm max}$ scaling relation not including a molecular weight term (Viani et al. 2017).

Other authors have investigated low-metallicity asteroseismic masses and compared them against *Gaia*-derived masses (Zinn et al. 2019b); M4 cluster masses (Miglio et al. 2016; Tailo et al. 2022; Howell et al. 2022); and field stars (Valentini et al. 2019; Matsuno et al. 2021). These studies find mixed evidence for mass inflation at low metallicities. With our relatively large sample of low metallicity stars, we therefore revisit the issue of seismic scaling-based mass for the low metallicity regime.

We make a number of cuts to the data sample in order to investigate the asteroseismic mass vs. metallicity relation in an unbiased way. In Figure 10 we show our selection of the halo stars (V $\geq$ 220 kms^{-1}). To ensure that the stars with masses higher than expected are not the result of explainable factors we also make the following cuts: all stars with the evolutionary type 'RC' are removed as it is likely that the evolutionary states in this regime are wrong, because hot RC stars would not show oscillations. All stars with a mass > 1.6 $M_\odot$ are removed to reduce the likelihood of merger products. There is also the recognition that there are asteroseismic biases in the highly luminous stars, so we remove stars with R > 30$R_\odot$ (Mosser et al. 2013; Stello et al. 2014; Kallinger et al. 2018; Zinn et al. 2019b, 2023). Finally, we remove stars with a fractional mass error (δM/M) > 0.15.

Initially, we plotted our stars using the calibrated temperatures from APOGEE (top plot in Figure 11). The calibrated spectroscopic temperatures available in APOGEE are calibrated to González Hernández & Bonifacio (2009). Full details are available in Holtzman et al. (2018). In order to evaluate the asteroseismic mass scale, we compare to masses inferred from Dartmouth isochrones (Dotter et al. 2008) with α-enhancement of [α/Fe] = 0.4, which is an upper bound of the α-enhancement at low metallicities; adopting a lower bound of [α/Fe] = 0.2 would lower the isochronal mass scale by less than 2%.[11]

The APOGEE-adopted IRFM scale (González Hernández & Bonifacio 2009) was anchored on a small sample of metal-poor stars, and so it is plausible that there are systematics in the temperature calibration at low metallicity. We therefore considered the effect of using the uncalibrated, ionization balanced temperatures from APOGEE. Plotting the stars using the uncalibrated temperatures (bottom plot in Figure 11) we found much better agreement with the older isochrones (10 and 14 Gyr); this indicates that temperature calibration may be a key factor in the resulting mass values at low metallicities, with much of the mass shift resulting indirectly from the temperature dependence of $f_{\Delta\nu}$.

Figure 12 shows the weighted median masses plotted with the Dartmouth isochrones, without the data points. This plot clearly shows the improved agreement for the asteroseismic masses derived using the uncalibrated APOGEE temperatures (red curve).

We compare the asteroseismic masses to the isochrone masses for each data point by subtracting the 10 Gyr isochrone mass from the uncalibrated and calibrated mass values and then finding the weighted means. The weighted average mass difference is 12.4% ±(4.5% (stat.) + 6% (syst.) for the calibrated masses and 2.9% ± 2.8% (stat.) + 6% (syst.) for the uncalibrated masses,

[11] In Section 3.5 we use MIST models instead of the Dartmouth isochrones used here. The use of Dartmouth at this point was to allow for an α-enhancement factor that was not necessary for the AGB cut.

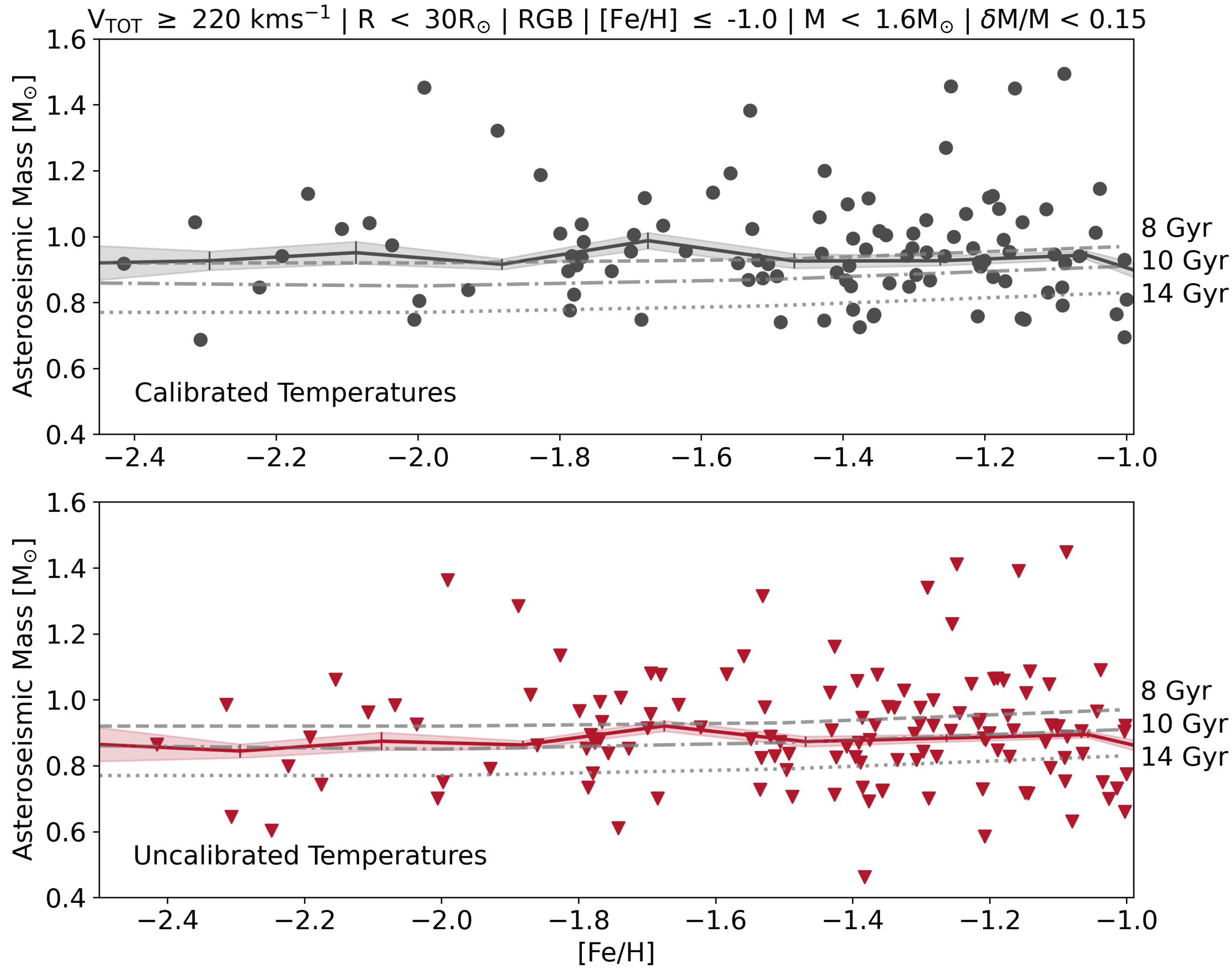

Figure 11. Weighted median asteroseismic mass [$M_\odot$] as a function of APOGEE [Fe/H] [dex], calculated using asteroseismic scaling relations and mass and radius coefficients (as discussed in Section 2.2). Dartmouth isochrones are shown by grey lines and labelled with their ages to the right of the plots (8 Gyr, 10 Gyr, and 14 Gyr). The black points in the top plot represent masses derived using calibrated temperatures from APOGEE and the existence of so many black points above the isochrone lines demonstrates the existence of potential overestimates in asteroseismic mass for the low-metallicity regime. Red triangles in the bottom plot represent masses calculated using the uncalibrated temperatures from APOGEE. The title shows cuts made to this plot (e.g., halo and RGB stars only). Binned medians of both samples have been added using a black (red) line on the top (bottom) plot with 1σ errors shown by the shaded regions.

in the sense of asteroseismic masses being larger than isochronal masses. The 6% systematic errors added to these values are due to the 2% uncertainty on the $\nu_{\rm max}$ scale. Performing the same calculations with the 14 Gyr isochrone values gives results of 20.6% ± 4.5% (stat.) + 6% (syst.) and 11.1% ± 2.8% (stat.) + 6% (syst.). If we consider the 14 Gyr isochrone as the true age, the masses could thus be 8.2% more inflated (for both the calibrated and uncalibrated temperature scales). Running these masses again with a weighted median, which is less sensitive to outliers, did not significantly change the result.

Two mass limits on this plot are of particular interest considering the precision of our asteroseismic masses. The first are the few RGB stars at $M < 0.8\ M_\odot$, which corresponds to the approximate minimum mass of an RGB star at the current age of the Galaxy (see mass for 14 Gyr isochrone with Dartmouth). These stars may have undergone mass loss throughout their evolution and represent interesting future studies. Conversely, 1.6 $M_\odot$ corresponds to the maximum possible mass (the maximum merger mass of two 0.8 $M_\odot$ stars). The RGB stars above this limit, although removed in the Figure 11, warrant further follow-up as they could represent

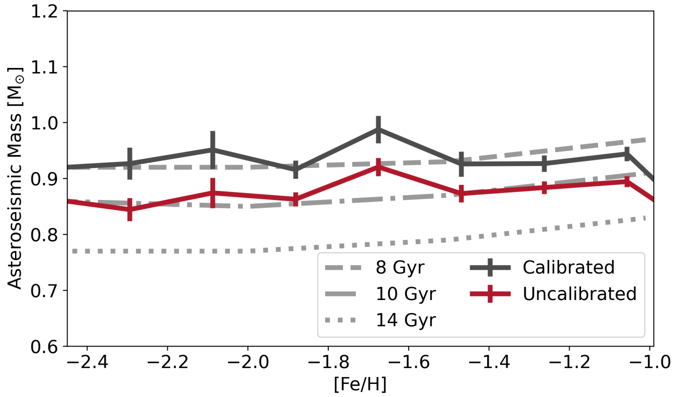

Figure 12. Asteroseismic mass [M$_\odot$] as a function of APOGEE [Fe/H] [dex]. Similar to Figure 11 but excluding the scatter plot. Grey lines correspond to Dartmouth isochrones at 8 Gyr (solid), 10 Gyr (dashed), and 14 Gyr (dotted).

interaction products.

4.2. *[α/Fe]-Bimodality*

An important abundance relation for exploring chemical enrichment in the Milky Way is the [α/Fe]-bimodality. This association compares α process elements (e.g., O, Mg, Ca, and Si) to Fe abundance in stellar populations, which results in two groups, clearly separable on a plot of [Fe/H] vs. [α/Fe], called the high- and low-[α/Fe] stars.

There are multiple theories about the origin of this double sequence. It has been suggested that the stars with larger α abundance form under different circumstances than the low-[α/Fe] stars (Mackereth et al. 2018). An enhanced α with high Fe suggests that the majority of the heavy elements come from core-collapse SNe, whilst a low-[α/Fe] mixture arises from a combination of SNe Ia and core-collapse SNe. The low-[α/Fe] stars tend to be young, reside in the thin disk, and form their own sequence. One possibility is that they result from decreased star formation efficiency as the Galaxy ages (Nidever et al. 2014); they also show different birth radii and an anti-correlation between angular momentum and [Fe/H], which suggests the existence of radial migration could be needed to form the sequence (Sharma et al. 2021); the effects of radial migration on the bimodality are also seen with the inward migration of super-solar metallicity stars in the solar-vicinity thin disc $R_{\rm Gal}$ = 7 - 9 kpc (Anders et al. 2017). The old, high-[α/Fe] stars generally reside in the thick disk; they display enhanced α abundance, sometimes low metal abundance, and are relatively kinematically hot (e.g., Haywood et al. 2013). These stars are thought to form from intense episodes of star formation, wherein the interstellar medium is dominated by the ejecta of core-collapse supernova. The [α/Fe]-bimodality has been seen both in the solar neighbourhood and beyond (Hayden et al. 2017); recent studies using asteroseismic ages find the age distribution for high- and low-[α/Fe] stars converge with increasing distance from the Galactic plane, (Warfield et al. 2021).

Our K2 data allows investigation of the [α/Fe]-bimodality. Figure 13 shows the α-bimodality plot for our sample. Asteroseismic masses are defined as in Section 2.2 and abundance information is taken from APOGEE. The eccentricity is defined in Section 4.3.

Our data extends the abundance ranges to lower metallicities, higher α abundances, and farther distances than *Kepler*. The APO-K2 sample offers a sample with asteroseismic masses including a known selection function to build on existing asteroseismic catalogs (e.g., Rendle et al. 2019; Mackereth et al. 2019b; Imig et al. 2022).

Using the asteroseismic mass as a proxy for age, we can see a clump of higher mass stars in the low-[α/Fe] regime, suggesting these stars are generally younger. Using the size of the marker (scaled for ease to the reader) to represent eccentricity and see that the highest eccentricity stars generally have high [α/Fe]-abundance and low metallicity.

Our sample adds over 1,000 stars to the [α/Fe]-bimodality plot as compared to the APOKASC-2 sample (∼6,000 stars), extending to lower metallicities and higher [α/Fe] abundance, allowing us to more clearly separate the high- and low-[α/Fe] samples. Figure 14 shows both the APOKASC-2 and APO-K2 catalogs over-plotted in metallicity-[α/Fe], illustrating the extent to which the APO-K2 catalog has expanded on the *Kepler* field, and confirming the convergence of the bimodality into a single distribution at higher metallicities.

Warfield et al. (2021) explored this space in K2 C4, C6, and C7, and discovered overlap between high- and low-α populations with stars of similar age. This discussion will continue in the companion paper of ages for this sample (Warfield et al. in prep.).

4.3. *Kinematics*

The *Gaia-Encaledus-Sausage* (GES) structure is thought to represent the remnants of a dwarf galaxy that merged with the Milky Way in its early history (Belokurov et al. 2018; Helmi et al. 2018; Montalbán et al. 2021). Though initially identified by kinematics, GES can also be identified by its combination of low metal-

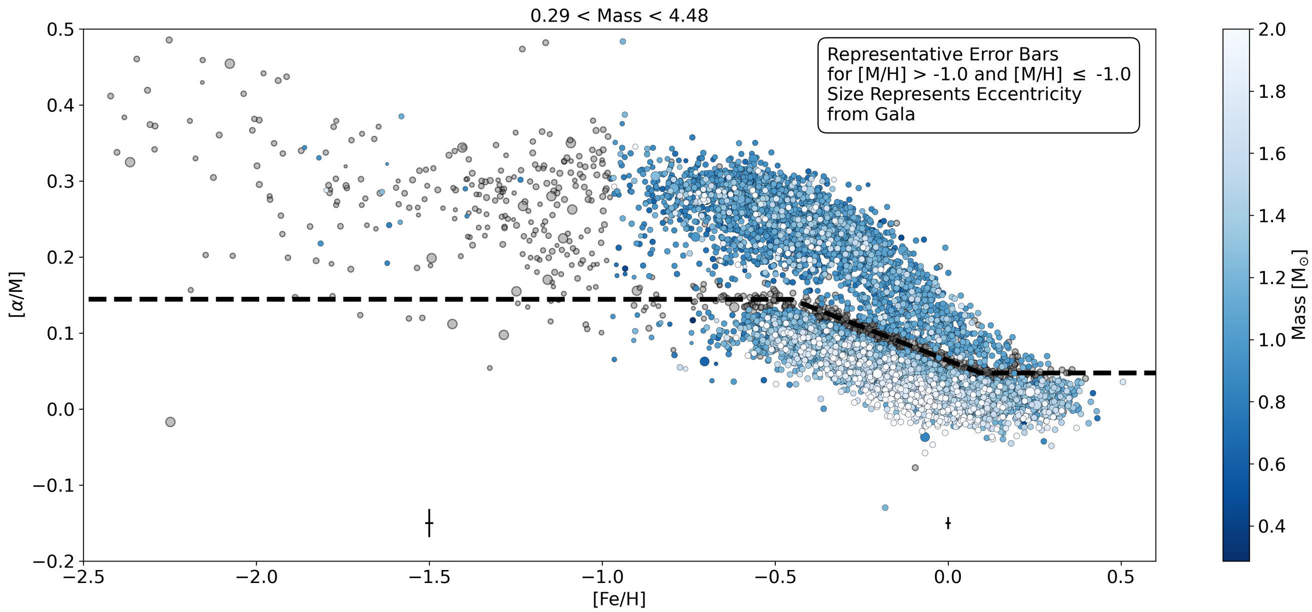

Figure 13. [α/Fe]-bimodality plot with the metallicity [Fe/H] ([α/Fe]) on the x-axis (y-axis). Color scale represents the asteroseismic mass [M$_\odot$], which has been truncated for clarity, with the full range of masses show in the title. Grey points correspond to stars with an alpha flag of -1.

The darker blue colors correspond to lower masses, with the data sorted by mass so that higher mass stars appear on the top. The size of each marker represents the Galactic eccentricity from `Gala`, which have been scaled for clarity to the reader. A dividing line is drawn to separate the low- and high-[α/Fe] stars, and this separation results in the flag contained in the APO-K2 catalog. Representative error bars are shown for both the relatively high and relatively low metallicity stars, where the separation occurs at [Fe/H] = -1.0.

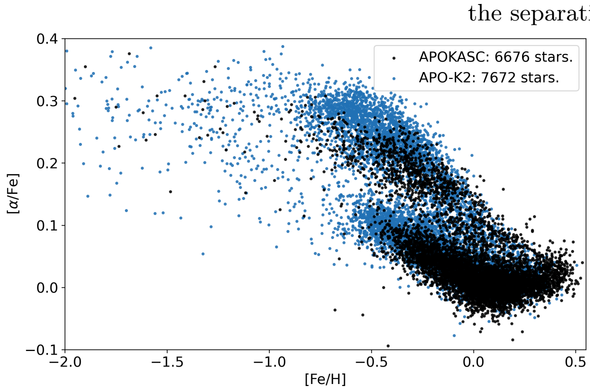

Figure 14. α-bimodality plot for both APOKASC-2 (grey) and APO-K2 (blue) overplotted to highlight the increase of sample size in this parameter space.

licity and particular abundance pattern (Haywood et al. 2018; Mackereth et al. 2019b).

To define the dynamical information for our sample we use `Gala` (Bovy 2015; Price-Whelan et al. 2017), an `Astropy`-affiliated (Astropy Collaboration et al. 2013, 2018) `Python` package. `Gala` uses the `Astropy` Galactocentric frame parameters adopted in `Astropy` v4.0. These are defined with a solar position of $R_\odot = 8.122$ kpc and $z_\odot = 20.8$ pc. The velocity of the Sun in the Galactocentric frame is (U, V, W)$_\odot$ = (12.9, 245.6, 7.78) km/s, as measured from Sgr A*. For our analysis we adopt the Milky Way Potential (`MilkyWayPotential`) available with `Gala`, using the default parameters of Milky Way mass, virial radius etc. The circular velocity at the Sun's position for the adopted potential is 231.5 km/s. `Gala` employs proper motions, parallax (distance) and radial velocities, with their associated errors, in its calculations of stellar orbital parameters. In Table 4 we provide the kinematic information for our stars including *Gaia* DR3 parallaxes corrected according to the *Gaia* zero point[12], evaluated using the `Python` implementation of the Lindegren et al. (2021) correction, and uncertainties [mas] according to El-Badry et al. (2021). We also include a DR3 binary flag, which will be nonzero if either of the following are true: the star is flagged in the `non_single_star` column of DR3 or the `fidelity_v2` value from Rybizki et al. (2022) is ≤ 0.5 or unavailable. All other parameters included in Table 4 are described in Section 3.2.

[12] https://gitlab.com/icc-ub/public/gaiadr3_zeropoint/-/tree/master

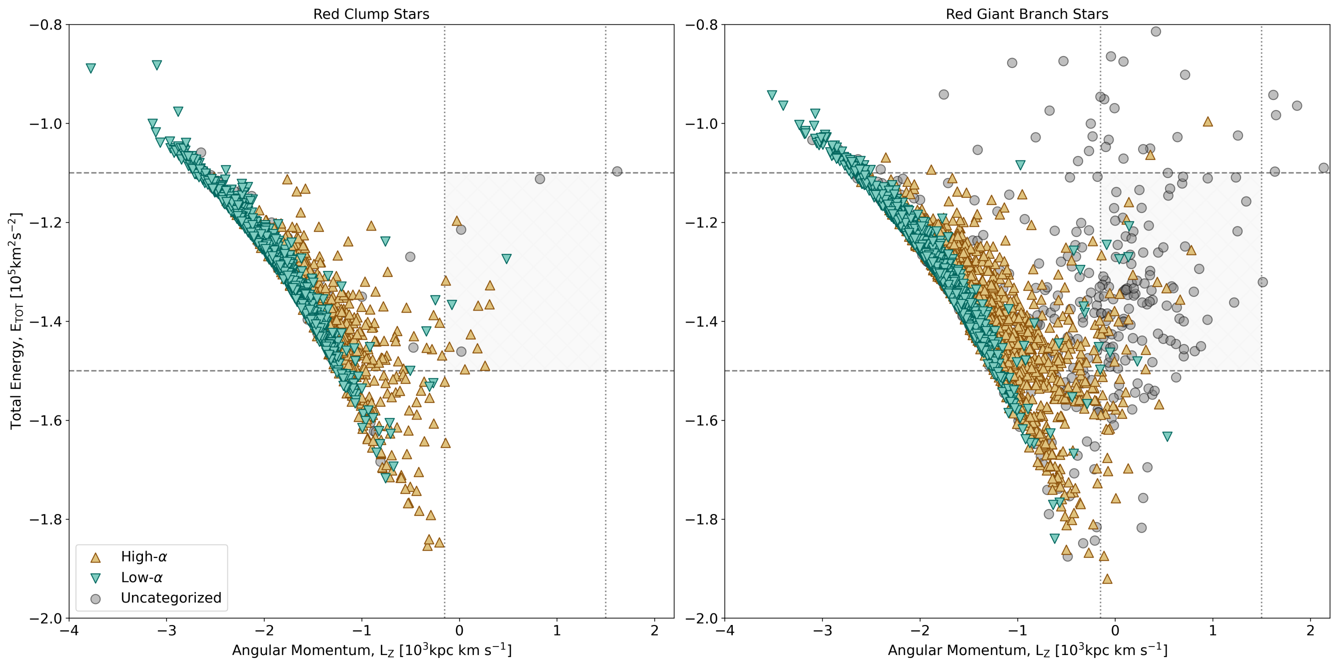

Figure 15. Kinematic plots for the APO-K2 sample. The plot on the left (right) corresponds to RC stars (RGB stars). Only stars with positive *Gaia* parallaxes are plotted. The grey area of the plots correspond to the area likely to host GES stars, and are defined by the lines drawn (and stated in the text). In both of these plots, the gold (green) stars correspond to the high-[α/Fe] (low-[α/Fe]) stars, as defined by Figure 13, and stars shown in grey are uncategorized (i.e., have an alpha flag of -1).

In Section 4.2 we used eccentricities (e) from `Gala` defined as

$$e = \frac{r_{apo} - r_{peri}}{r_{apo} + r_{peri}}, \tag{9}$$

where r_{apo} is the orbital apocentre and r_{peri} is the orbital pericentre.

To derive the orbital parameters of eccentricity and $|Z_{\rm max}|$ we created 100 instances of each star, and used `Pyia`[13] and `Gala` to integrate their orbits over 5000 steps with a time step of 0.8Myr. The values for each star were then determined using the mean value from the 100 iterations, and errors were calculated using the standard deviation of the measurements. We note that the uncertainty of $|Z_{max}|$ increases with the Galactic radii of the star, so for those stars with large $|Z_{max}|$ values, these orbital parameters may not be accurate. Velocities, total energy, and angular momentum for each star were computed in much the same way.

Figure 15 shows orbital angular momentum (L_z) [10^3 kpc km/s] as a function of total energy ($E_{\rm TOT}$) [10^5 km^2 s^{-2}]. This space is most often used to identify merger debris from past accretion events. Colors correspond to the relative α-abundance with high-[α/Fe] (gold) and low-[α/Fe] (green), based on the alpha flag provided in the catalog. We also show the stars with an alpha flag of -1 as grey circles. We display the sample broken down by evolutionary state (RGB and RC), with boundaries for the GES overlaid. The vertical lines denote the GES limits in angular momentum from Helmi et al. (2018), between $-150 < L_z$ [kpc kms^{-1}] < 1500. The GES distinction in total energy is taken from Koppelman et al. (2019) and placed between $-1.1{\times}10^5$ km^{2}s^{-2} and $-1.5{\times}10^5$ km^{2}s^{-2}. Inside the grey box lie a few dozen GES substructure candidates.

Figure 15 shows the low-[α/Fe] stars mainly occupy the disk, and hence are seen in fairly circular orbits that sit close to the curve that defines the minimum energy given the Milky Way potential. By contrast, the high-[α/Fe] stars, residing mainly in the thick disk and halo are expected to be kinematically hot (possessing eccentric orbits) and occupy more diffusely the region above the minimum energy curve.

Koppelman et al. (2019) discuss the necessity of a chemical tagging analysis to determine whether substructures are related to accretion events. They studied the distribution of nearby thick disk and halo stars using 6D phase-space data from *Gaia* DR2 and found that not all substructure is due to accretion, nor is it due to the settling of the gravitational potential after major activity (Haywood et al. 2018). The range of kinematic

[13] https://pyia.readthedocs.io/en/latest/#

parameter space probed in this sample may prove useful for future analysis, in combination with the selection functions presented in S22.

5. CONCLUSIONS

In this paper we summarize the APO-K2 evolved star sample, with corresponding spectroscopic (APOGEE DR17), asteroseismic (K2-GAP), and astrometric (*Gaia* EDR3) parameters. Our sample of 7,672 unique stars contains RGB, RC, secondary red clump, and RGB bump evolutionary states, from various areas of the Galaxy. Our work provides precise asteroseismic radii and masses as well as evolutionary states and metallicities, explored in multiple parameter spaces.

Throughout this work, we overviewed many parameter spaces that our catalog extends, some for the first time. We investigate the completeness of our sample by comparing it to the S22 selection function, in the mass-radius, mass-metallicity, color-magnitude, and magnitude-$\nu_{\rm max}$ regimes. The large sample of red giants presented here results in a significant number of intrinsically rare objects, like secondary clump stars, which are promising for stellar physics tests. We examine our astereosismic masses in the low-metallicity regime, resulting in higher masses than expected for the low-metallicity stars, even when taking corrections to the $\Delta\nu$ scaling relation into account. We find that using raw APOGEE temperatures to derive stellar masses results in a better agreement with astrophysical estimates for very metal-poor stars. We also show that these low-metallicity stars dramatically increase the number of stars available in the high-α population compared to *Kepler* asteroseismic samples. Finally, we looked at our sample in kinematic space, with *Gaia* DR3, and identified potential GES stars. The chemical properties of potential GES members is an interesting topic — we have identified potential GES members in order to advertise the importance of this catalogue for Galactic evolution studies, and we leave the detailed abundances patterns of the kinematics-selected GES candidate members to a separate work in preparation (Schonhut-Stasik et al. in prep.).

The overview presented in our paper only scratches the surface of the rich data sample; some of the spaces explored in this paper will be further investigated in follow-up papers. Further work will be undertaken to explore the multiplicity (Schonhut-Stasik et al. in prep.), and abundance space provided by APOGEE (Schonhut-Stasik et al. in prep.), for example, to investigate the carbon-enhanced stars known to exist at low metallicity (e.g., Beers & Christlieb 2005; Suda et al. 2008), and the young high-/*alpha* population (Chiappini et al. 2015). A companion paper will release age information for the APO-K2 catalog (Warfield et al. in prep.).

The amount of stars accessible to Galactic archaeology using asteroseismology will only grow with future missions. For example, the NASA planet-finding mission TESS (Ricker et al. 2014; Hon et al. 2022) and the Nancy Grace Roman Telescope (Gould et al. 2015; Spergel et al. 2015), as well as the ESA missions Euclid (Laureijs et al. 2011; Gould et al. 2016) and PLATO (Rauer et al. 2014; Miglio et al. 2017), will yield enormous harvests of asteroseismic detections. In terms of spectroscopic measurements, the upcoming projects WEAVE (Dalton et al. 2020), MOONS (Cirasuolo et al. 2014), and 4MOST (de Jong et al. 2012) will increase chemical abundance yields. Finally with future releases from *Gaia*, our astrometry and kinematic data will only increase in precision.

ACKNOWLEDGEMENTS

We would like to thank the community that supports APO-K2. J.S.S. is supported a Neurodiversity Inspired Science and Engineering (NISE) Fellowship under award. J.C.Z. was supported by an NSF Astronomy and Astrophysics Postdoctoral Fellowship under award AST-2001869. D.M. gratefully acknowledges support by the ANID BASAL projects ACE210002 and FB210003 and by Fondecyt Project No. 1220724. S.M. acknowledges support from the Spanish Ministry of Science and Innovation (MICINN) with the Ramón y Cajal fellowship no. ~RYC-2015-17697, grant no. PID2019-107187GB-I00 and PID2019-107061GB-C66 for PLATO, and through AEI under the Severo Ochoa Centres of Excellence Programme 2020–2023 (CEX2019-000920-S). D.S. acknowledges support from the Australian Research Council Discover Project DP190100666. R.A.G. and B.M. acknowledge the support from the PLATO Centre National D'Études Spatiales grant. DM also acknowledges support from CNPq/Brazil through project350104/2022-0

This paper includes data collected by the *Kepler* mission and the K2 mission. Funding for the *Kepler* mission and K2 mission are provided by the NASA Science Mission directorate.

This work has made use of data from the European Space Agency (ESA) mission *Gaia* (https://www.cosmos.esa.int/gaia), processed by the*Gaia* Data Processing and Analysis Consortium (DPAC, https://www.cosmos.esa.int/web/gaia/dpac/consortium). Funding for the DPAC has been provided by national institutions, in particular the institutions participating in the *Gaia* Multilateral Agreement. This research has made use of the VizieR catalogue access tool, CDS, Stras-

EPIC ID	APOGEE ID	Gaia DR3 ID	Campaign	RA [deg]	Dec [deg]	b [deg]	l [deg]	Evol	T_{eff} [K]	$\sigma_{T_{eff}}$ [K]	$\log(g)$ [dex]	$\sigma_{\log(g)}$ [dex]
211705076	2M08374542+1558546	657961231375051264	5, 16, 18	129.4393	15.9818	30.56	209.68	RGB	4664	7	2.872	0.021
212873074	2M13305142-0302596	3637132654493312512	17	202.7143	-3.0499	58.36	321.95	RGB	4789	11	2.782	0.029
204651310	2M16593864-2127129	4126325130252374528	11	254.911	-21.4536	12.79	0.4	RGB	4667	7	3.027	0.02
212386819	2M13364485-1513074	3606298775037819392	6	204.1869	-15.2187	46.25	318.84	RC	4761	8	2.474	0.022
228774437	2M12441419-0751315	3675439948842715648	10	191.0591	-7.8588	54.97	299.82	RC	5006	9	2.847	0.021
212349887	2M13394793-1608035	3605235169336614400	6	204.9497	-16.1343	45.17	319.52	RC	4828	9	2.457	0.024
204970434	2M16494197-2001358	4130505439095442944	2	252.4249	-20.0266	15.51	0.14	RGB	4827	14	2.415	0.035
228909546	2M12254205-0306337	3693228260274665472	10	186.4252	-3.1094	59.13	290.33	RC	4725	8	2.378	0.022
201698245	2M11284829+0336340	3812520972624745472	1	172.2012	3.6095	59.3	259.34	RGB	4665	10	2.239	0.032
201495451	2M10544228+0027166	3804835077108840448	14	163.6762	0.4546	51.32	251.66	RC	4662	7	2.43	0.021
206384822	2M22300191-0652342	2622798470238605312	3	337.508	-6.8762	-50.83	57.51	RGB	4179	5	1.824	0.02
247512035	2M05024943+2217174	3418251294206034944	13	75.706	22.2882	-11.71	180.16	RC	4677	7	2.433	0.021
211623551	2M08413695+1451547	609605736481635200	5, 16, 18	130.404	14.8652	30.98	211.29	RC	5032	10	2.757	0.022
251566284	2M13291268-0202116	3638370116175271936	17	202.3029	-2.0366	59.45	321.75	RGB	4941	9	2.975	0.023
248856910	2M10595542+1204552	3871633230290062336	14	164.981	12.082	59.85	237.38	RGB	4800	8	2.49	0.022
212328705	2M13362612-1642100	3603874691200483328	6	204.1088	-16.7028	44.83	318.21	RGB	4806	9	2.592	0.025
228902151	2M12271983-0314176	3693539215906675712	10	186.8326	-3.2382	59.08	291.16	RC	4958	10	2.426	0.027
212342710	2M13353650-1619290	3603970421727041024	6	203.9021	-16.3247	45.25	318.07	RC	4699	7	2.445	0.021
211342712	2M08532503+1040506	598595708076959872	5	133.3543	10.6807	31.89	217.15	RGB	4638	7	2.214	0.023
248833327	2M11001398+1129143	3871457922609751040	14	165.0583	11.4873	59.58	238.43	RGB	4582	7	2.584	0.024
211418744	2M08501827+1155212	604967244817098240	[5, 16, 18]	132.5762	11.9226	31.73	215.45	RC	4743	8	2.353	0.023
248828012	2M10575784+1121231	3871441365511075840	14	164.491	11.3564	59.04	238.02	RC	4725	8	2.444	0.022
247487137	2M04574880+2205410	3412369491113446912	13	74.4534	22.0947	-12.75	179.61	RC	4844	9	2.498	0.024
211380313	2M08521656+1119380	604696730596495744	5, 18	133.069	11.3272	31.91	216.32	RGB	4391	6	2.122	0.021
228973349	2M12283232-0158166	3693965688979458048	10	187.1347	-1.9713	60.38	291.29	RC	4879	9	2.51	0.025
212357017	2M13374476-1556555	3605438063591567872	6	204.4365	-15.9488	45.48	318.91	RGB	4729	8	2.928	0.02
204964919	2M16461562-2003089	4130449814981629952	2	251.5651	-20.0525	16.14	359.61	RGB	4560	9	2.714	0.024
251541831	2M13223736-0235249	3638103763778784768	17	200.6557	-2.5903	59.35	318.34	RC	4922	9	2.628	0.023
247418635	2M05021404+2132500	3409186130072687616	13	75.5585	21.5472	-12.25	180.69	RGB	4386	6	1.96	0.021
248404489	2M10501626-0016330	3806259563141801472	14	162.5678	-0.2758	50.02	251.21	RGB	4217	5	1.991	0.019
...	...	...	...	...	...	...	...	...	...	...	...	...

Table 1. This table contains basic positional and stellar parameter data for each of the stars in the APO-K2 catalog. The EPIC ID, APOGEE ID, and Gaia EDR3 ID are given in the first three columns and drawn from their respective catalogs. The Campaign number(s) corresponds to the K2 campaign of observation; if the star was observed in more than one campaign then all campaigns are listed. The RA and Dec are given in degrees as are the Galactic latitude and longitude. The 'Evol' column contains the derived evolutionary state of the star with 'RC' corresponding to red clump stars and 'RGB' corresponding to red giant branch stars. The T_{eff} [K] and σT_{eff} [K] columns provide the calibrated effective temperatures from APOGEE and the $\log(g)$ [dex] and $\sigma \log(g)$ [dex] columns are the calibrated surface gravities from APOGEE.

EPIC ID	$\nu_{\max}$ [μHz]	$\sigma\nu_{\max}$ [μHz]	$\Delta\nu$ [μHz]	$\sigma\Delta\nu$ [μHz]	$f_{\Delta\nu}$	$\sigma f_{\Delta\nu}$	$f_{\Delta\nu}$ Flag	$\kappa_{\rm M}$	$\sigma\kappa_{\rm M}$	Mass [$M_\odot$]	σMass [$M_\odot$]	$\kappa_{\rm R}$	$\sigma\kappa_{\rm R}$	Radius [$R_\odot$]	σRadius [$R_\odot$]
211705076	98.008	0.574	9.267	0.091	1.024	0.0008	0	1.463	0.063	1.061	0.069	6.776	0.139	6.089	0.125
212873074	49.941	0.411	5.198	0.019	1.0261	0.0009	0	1.955	0.056	1.476	0.05	10.974	0.121	9.992	0.111
204651310	148.608	1.503	12.949	0.032	1.0158	0.0012	0	1.338	0.043	0.971	0.033	5.262	0.059	4.73	0.053
212386819	32.987	1.205	3.952	0.069	0.9978	0.0006	0	1.686	0.219	1.262	0.196	12.54	0.634	11.385	0.575
228774437	89.247	1.575	7.56	0.093	0.9932	0.0005	0	2.495	0.18	2.012	0.189	9.273	0.281	8.632	0.261
212349887	31.614	0.702	3.97	0.035	0.9981	0.0007	0	1.457	0.11	1.113	0.097	11.908	0.338	10.886	0.309
204970434	25.992	0.701	2.979	0.036	1.0214	0.0023	0	2.554	0.241	1.951	0.217	17.386	0.63	15.892	0.576
228909546	31.082	0.639	3.69	0.153	0.9972	0.0009	0	1.857	0.329	1.374	0.37	13.557	1.158	12.261	1.048
201698245	27.508	0.835	3.05	0.115	1.0242	0.0057	0	2.757	0.486	2.0	0.511	17.558	1.427	15.778	1.283
201495451	32.034	0.489	4.081	0.039	0.9984	0.0004	0	1.359	0.081	0.985	0.075	11.423	0.279	10.262	0.251
206384822	11.93	0.295	1.951	0.011	1.0444	0.0018	0	1.343	0.104	0.826	0.068	18.61	0.506	15.827	0.43
247512035	33.972	0.707	4.218	0.063	0.9983	0.0004	0	1.42	0.123	1.034	0.117	11.339	0.413	10.202	0.372
211623551	90.875	1.456	7.487	0.065	0.9932	0.0005	0	2.738	0.162	2.225	0.163	9.626	0.227	8.984	0.212
251566284	133.479	1.389	10.884	0.136	1.0116	0.0008	0	1.943	0.114	1.536	0.131	6.691	0.181	6.188	0.168
248856910	39.742	0.658	3.662	0.029	1.0025	0.0031	0	4.0	0.236	3.029	0.214	17.595	0.403	16.038	0.368
212328705	54.207	0.785	5.761	0.039	1.0272	0.0007	0	1.657	0.085	1.257	0.077	9.696	0.192	8.844	0.176
228902151	30.078	1.011	4.233	0.125	0.9932	0.0079	0	0.971	0.151	0.772	0.164	9.967	0.677	9.233	0.627
212342710	36.614	0.648	4.274	0.061	0.9977	0.0004	0	1.686	0.131	1.237	0.13	11.9	0.4	10.733	0.361
211342712	16.67	0.867	2.347	0.004	1.0305	0.0016	0	1.749	0.273	1.258	0.197	17.963	0.936	16.094	0.839
248833327	42.672	0.279	5.133	0.038	1.0352	0.0004	0	1.283	0.046	0.907	0.046	9.618	0.156	8.566	0.139
211418744	26.583	0.443	3.286	0.051	0.9992	0.0003	0	1.846	0.147	1.374	0.151	14.616	0.515	13.244	0.467
248828012	31.432	1.087	4.065	0.211	0.998	0.0033	0	1.304	0.303	0.964	0.332	11.296	1.236	10.216	1.118
247487137	36.982	1.312	4.165	0.043	0.995	0.0009	0	1.927	0.22	1.479	0.185	12.659	0.52	11.592	0.476
211380313	15.885	0.283	2.169	0.059	1.0315	0.003	0	2.075	0.251	1.375	0.248	20.044	1.147	17.476	1.0
228973349	35.42	0.321	4.342	0.079	0.9976	0.0005	0	1.433	0.111	1.113	0.132	11.157	0.418	10.253	0.385
212357017	108.613	1.046	9.474	0.061	1.0187	0.0006	0	1.823	0.071	1.35	0.067	7.185	0.116	6.501	0.105
204964919	64.729	1.655					2								
251541831	43.795	0.574	4.63	0.022	0.9937	0.0005	0	2.096	0.092	1.648	0.082	12.133	0.196	11.199	0.182
247418635	10.032	0.165	1.489	0.191	1.0287	0.0202	0	2.357	1.215	1.559	1.268	26.884	6.913	23.425	6.024
248404489	16.014	0.45	2.389	0.014	1.0416	0.002	0	1.444	0.126	0.9	0.083	16.654	0.507	14.228	0.433
...	...	...	...	...	...	...	...	...	...	...	...	...	...	...	...

Table 2. Table contains the asteroseismic values for the stars in the sample. From left to right we provide the frequency of maximum power ($\nu_{\max}$) [μHz], large frequency separation ($\Delta\nu$) [μHz], the $\Delta\nu$ correction factor ($f_{\Delta\nu}$), and the $f_{\Delta\nu}$ flag. Note that the $\Delta\nu$ values provided here have already had the $f_{\Delta\nu}$ applied and therefore are not needed in Equations 1 and 2. Explanation of this flag can be found in Section 3.2. We also include the asteroseismic mass and radius coefficients, along with the stellar mass [$M_\odot$] and stellar radius [$R_\odot$] computed when using these values with the APOGEE temperatures, and their associated errors.

EPIC ID	[M/H] [dex]	$\sigma_{[M/H]}$ [dex]	[Fe/H] [dex]	$\sigma_{[Fe/H]}$ [dex]	[α/M]	$\sigma_{[\alpha/M]}$	α-Flag	V_{mag} [mag]	$\sigma_{V_{mag}}$ [mag]	J [mag]	σ_J [mag]	K_s [mag]	σ_{K_s} [mag]	J-K_s	σ_{J-K_s}
211705076	0.0019	0.006	-0.0087	0.0072	0.072	0.005	-1	9.402	0.875	7.555	0.02	6.913	0.026	0.642	0.033
212873074	-0.2655	0.0084	-0.2752	0.0098	0.0575	0.0079	0	7.027	0.812	5.143	0.017	4.488	0.036	0.655	0.04
204651310	0.1912	0.0055	0.1745	0.0068	0.0274	0.0044	0	9.782	0.788	7.647	0.019	6.91	0.018	0.737	0.026
212386819	-0.0508	0.006	-0.0572	0.0071	0.01	0.0053	0	9.494	0.824	7.644	0.019	7.001	0.024	0.643	0.031
228774437	0.0398	0.0056	0.032	0.0065	-0.0191	0.0052	0	9.181	0.842	7.536	0.026	6.968	0.023	0.568	0.035
212349887	-0.2352	0.0064	-0.2454	0.0074	0.0469	0.0061	0	9.756	0.93	7.78	0.026	7.094	0.02	0.686	0.033
204970434	-0.4503	0.01	-0.4612	0.0115	0.2651	0.0101	1	13.355	1.235	11.327	0.023	10.624	0.021	0.703	0.031
228909546	-0.0284	0.006	-0.0343	0.0072	-0.0026	0.0052	0	9.507	0.918	7.555	0.026	6.877	0.021	0.678	0.033
201698245	-0.6215	0.0091	-0.6287	0.0103	0.2823	0.0092	1	12.718	1.122	10.769	0.022	10.092	0.021	0.677	0.03
201495451	0.0292	0.0059	0.0166	0.0072	0.0114	0.0049	0	10.013	1.122	7.97	0.027	7.262	0.026	0.708	0.037
206384822	0.1197	0.0061	0.1094	0.0078	0.0864	0.0042	1	11.795	1.288	9.338	0.022	8.508	0.023	0.83	0.032
247512035	0.0788	0.0058	0.072	0.007	-0.003	0.0048	0	10.534	1.03	8.066	0.023	7.233	0.017	0.833	0.029
211623551	-0.0557	0.0058	-0.056	0.0067	-0.0197	0.0056	0	9.99	0.804	8.451	0.026	7.925	0.018	0.526	0.032
251566284	-0.0918	0.0059	-0.0934	0.0069	0.0327	0.0057	0	9.797	0.869	8.056	0.019	7.452	0.026	0.604	0.032
248856910	-0.001	0.0058	-0.0074	0.007	0.0142	0.0052	0	10.136	1.076	8.205	0.026	7.534	0.026	0.671	0.037
212328705	-0.3587	0.0068	-0.3615	0.0077	0.0777	0.0067	0	9.872	1.046	7.947	0.029	7.278	0.023	0.669	0.037
228902151	-0.4721	0.0069	-0.4822	0.0077	0.1096	0.0074	0	9.75	1.171	7.993	0.035	7.383	0.027	0.61	0.044
212342710	0.0617	0.0058	0.0549	0.007	-0.0082	0.0049	0	10.328	1.074	8.349	0.024	7.662	0.026	0.687	0.035
211342712	-0.148	0.0064	-0.1552	0.0076	0.0319	0.0056	0	9.994	0.923	7.935	0.026	7.222	0.017	0.713	0.031
248833327	-0.2773	0.0068	-0.2961	0.008	0.1988	0.006	1	10.46	1.337	8.454	0.023	7.758	0.036	0.696	0.043
211418744	-0.1674	0.0063	-0.1749	0.0074	0.0238	0.0058	0	9.997	0.878	8.087	0.02	7.423	0.023	0.664	0.03
248828012	-0.0359	0.006	-0.0436	0.0072	0.0343	0.0052	0	10.552	0.939	8.665	0.021	8.009	0.023	0.656	0.031
247487137	-0.1926	0.0063	-0.1987	0.0073	0.0349	0.006	0	10.637	0.898	8.369	0.021	7.592	0.016	0.777	0.026
211380313	-0.0124	0.0062	-0.019	0.0077	0.0052	0.0048	0	10.072	0.92	7.875	0.023	7.119	0.018	0.756	0.029
228973349	-0.286	0.0065	-0.3033	0.0074	0.0633	0.0064	0	9.88	0.903	8.114	0.023	7.501	0.024	0.613	0.033
212357017	0.1313	0.0056	0.1253	0.0068	0.0039	0.0046	0	10.482	0.812	8.746	0.024	8.144	0.016	0.602	0.029
204964919	0.3467	0.0074	0.3219	0.0096	0.0244	0.0054	0	13.724	1.579	11.196	0.021	10.347	0.025	0.849	0.033
251541831	-0.1212	0.006	-0.1322	0.007	0.0202	0.0058	0	10.04	0.874	8.366	0.023	7.787	0.023	0.579	0.033
247418635	0.0323	0.0061	0.0167	0.0076	-0.0133	0.0047	0	10.706	1.23	7.76	0.023	6.809	0.017	0.951	0.029
248404489	0.1938	0.0059	0.1833	0.0075	0.0631	0.0041	1	11.041	1.185	8.532	0.019	7.688	0.024	0.844	0.031
...	...	...	...	...	...	...	...	...	...	...	...	...	...	...	...

Table 3. This table contains elemental abundance and magnitude information for each of the stars in the sample. The EPIC ID is used as the main identifier in this and subsequent tables. Metallicity is presented the form of both [M/H] [dex] and iron abundance [Fe/H] [dex], taken from APOGEE, with their corresponding errors. The α abundance [α/Fe] [dex] is also taken from APOGEE. An α flag is provided, and an explanation is given in Section 3.2. The V_{mag} [mag] color is calculated from Equation 5 with the error calculated using standard propagation of uncertainty. Also included are the J- and K_s-band magnitudes [mag] from the EPIC along with the J-K_s color, with their associated errors.

EPIC ID	ϖ [mas]	σ_ϖ [mas]	e	σ_e	$\|Z_{max}\|$ [kpc]	$\sigma_{\|Z_{max}\|}$ [kpc]	L_Z [10^3kpc km/s]	σ_{L_Z} [10^3kpc km/s]	E_{TOT} [10^5km^2/s^2]	$\sigma_{E_{TOT}}$ [10^5km^2/s^2]	U [km/s]	σ_U [km/s]	V [km/s]	σ_V [km/s]	W [km/s]	σ_W [km/s]	DR3 Flag
211705076	3.461	0.02	0.1815	0.0003	0.3807	0.0027	-1.761	0.0021	-1.3107	0.0005	42.95	0.19	-20.3	0.11	-23.85	0.13	1
212873074	6.812	0.033	0.1669	0.0002	0.171	0.0005	-2.1553	0.0006	-1.2094	0.0002	-14.14	0.05	35.11	0.04	1.52	0.11	0
204651310	4.492	0.018	0.0468	0.0005	0.1447	0.0006	-1.8019	0.0008	-1.3169	0.0002	-18.09	0.19	-4.28	0.02	8.23	0.05	0
212386819	1.911	0.022	0.1568	0.0003	0.4823	0.0006	-2.0743	0.0006	-1.2282	0.0003	0.11	0.08	32.22	0.08	7.26	0.11	0
228774437	2.298	0.019	0.0701	0.0003	0.3881	0.0002	-1.9035	0.0012	-1.2837	0.0003	-30.32	0.06	5.12	0.09	0.95	0.12	0
212349887	1.818	0.022	0.204	0.0006	0.4503	0.0009	-1.9458	0.0026	-1.2532	0.0005	-71.84	0.14	14.23	0.11	-3.16	0.18	0
204970434	0.407	0.02	0.3159	0.002	1.2523	0.0081	-0.983	0.0434	-1.5328	0.0156	-89.72	1.05	-59.57	0.18	-66.23	0.36	0
228909546	1.737	0.024	0.0537	0.0003	0.6553	0.0011	-1.9355	0.0006	-1.2723	0.0001	-13.68	0.06	8.85	0.08	18.0	0.12	0
201698245	0.406	0.019	0.3177	0.0028	3.592	0.019	-1.091	0.0456	-1.3769	0.0012	-47.89	0.2	-107.95	0.39	-95.19	0.63	0
201495451	1.803	0.02	0.1917	0.0005	0.4131	0.0003	-1.6493	0.0016	-1.3427	0.0002	-54.83	0.05	-33.83	0.11	-0.31	0.14	0
206384822	0.688	0.02	0.2196	0.0007	0.9477	0.0004	-1.3928	0.0124	-1.4106	0.0024	-2.96	0.13	-50.11	0.13	2.36	0.17	0
247512035	1.75	0.02	0.0379	0.0004	0.2467	0.001	-1.9701	0.0007	-1.2688	0.0002	6.43	0.15	-5.3	0.05	13.29	0.06	0
211623351	1.478	0.022	0.0454	0.0003	0.3824	0.0004	-1.9677	0.0008	-1.2677	0.0002	1.83	0.12	-3.63	0.09	3.84	0.11	0
251566284	2.683	0.023	0.2038	0.0001	0.3831	0.0001	-2.0522	0.0005	-1.2264	0.0004	43.47	0.06	25.91	0.05	-1.25	0.12	0
248856910	1.078	0.027	0.1301	0.0004	0.8584	0.0008	-1.9635	0.0024	-1.255	0.0003	23.9	0.11	3.72	0.11	-9.88	0.13	0
212328705	2.121	0.027	-999.0	-999.0		-999.0	-999.0	-999.0	-999.0	-999.0	-999.0	-999.0	-999.0	-999.0	-999.0	-999.0	0
228902151	1.673	0.019	0.148	0.0002	0.8763	0.0024	-1.6687	0.0017	-1.3348	0.0003	27.45	0.06	-22.71	0.08	33.56	0.13	0
212342210	1.464	0.021	0.1279	0.0003	0.5987	0.0009	-1.9301	0.0018	-1.2679	0.0003	15.41	0.1	17.27	0.09	-16.21	0.12	0
211342712	1.054	0.024	0.1276	0.0003	1.1991	0.0027	-1.8917	0.0009	-1.2682	0.0008	23.27	0.1	-14.79	0.08	42.69	0.09	0
248833327	1.664	0.025	0.3462	0.0004	0.729	0.0022	-1.3208	0.0057	-1.4041	0.0008	-55.83	0.07	-74.35	0.09	33.33	0.16	0
211418744	1.329	0.018	-999.0	-999.0		-999.0	-999.0	-999.0	-999.0	-999.0	-999.0	-999.0	-999.0	-999.0	-999.0	-999.0	0
248828012	1.209	0.018	0.1809	0.0004	0.7986	0.0008	-2.0093	0.0014	-1.2365	0.0003	38.54	0.09	10.4	0.1	-13.17	0.15	0
247487137	1.502	0.024	0.1907	0.0004	0.2011	0.001	-1.9287	0.0017	-1.263	0.0003	-62.87	0.16	-12.34	0.06	8.11	0.07	0
211380313	1.214	0.018	-999.0	-999.0		-999.0	-999.0	-999.0	-999.0	-999.0	-999.0	-999.0	-999.0	-999.0	-999.0	-999.0	0
228973349	1.517	0.025	0.0738	0.0004	0.6323	0.0002	-1.9701	0.0009	-1.2622	0.0002	-12.52	0.07	13.7	0.08	0.3	0.14	0
212357017	1.994	0.024	0.195	0.0002	0.4134	0.0002	-1.9521	0.0007	-1.2537	0.0003	44.67	0.1	17.71	0.08	0.35	0.12	0
204964919	0.598	0.02	0.2003	0.0023	0.4867	0.0008	-1.4372	0.0164	-1.412	0.0054	-67.91	0.8	-11.55	0.12	10.09	0.26	0
251541831	1.323	0.027	0.2332	0.0004	0.7839	0.0003	-2.0732	0.0009	-1.2101	0.0009	-66.81	0.11	30.46	0.1	3.68	0.16	0
247418635	1.219	0.027	0.1665	0.0005	0.2178	0.0012	-2.1155	0.0027	-1.2188	0.0007	-55.65	0.14	4.74	0.1	6.81	0.11	0
248404489	1.071	0.022	0.1185	0.0006	0.8223	0.0004	-2.1213	0.0032	-1.2178	0.0011	-21.57	0.11	21.76	0.15	2.28	0.15	0
...	...	...	...	...	...	...	...	...	...	...	...	...	...	...	...	...	...

Table 4. Table providing kinematic data for the catalog. Includes the EPIC ID that links all the tables. We then provide, in column order, the corrected *Gaia* DR3 parallaxes corrected according to the *Gaia* zero point, evaluated using the `Python` implementation of the Lindegren et al. (2021) correction, and uncertainties [mas] (according to El-Badry et al. (2021)). In the proceeding columns we give the `Gala`-defined parameters: the Galactic eccentricity, the maximum excursion of the orbit from the Galactic plane ($|Z_{max}|$) [kpc], the orbital angular momentum (L_z) [10^3 kpc km/s], the total orbital energy (E_{TOT}) [10^5 km^2 s$^-2$], and the U, V, and W velocities [km/s]. All these values are provided with their associated errors. Finally, we provide a DR3 binary flag, an explanation of which can be found in Section 3.2.

bourg, France (DOI: 10.26093/cds/vizier). The original description of the VizieR service was published Ochsenbein et al. (2000).

Funding for the Sloan Digital Sky Survey IV has been provided by the Alfred P. Sloan Foundation, the U.S. Department of Energy Office of Science, and the Participating Institutions. SDSS-IV acknowledges support and resources from the Center for High-Performance Computing at the University of Utah. The SDSS web site is www.sdss.org.

SDSS-IV is managed by the Astrophysical Research Consortium for the Participating Institutions of the SDSS Collaboration including the Brazilian Participation Group, the Carnegie Institution for Science, Carnegie Mellon University, the Chilean Participation Group, the French Participation Group, Harvard-Smithsonian Center for Astrophysics, Instituto de Astrofísica de Canarias, The Johns Hopkins University, Kavli Institute for the Physics and Mathematics of the Universe (IPMU) / University of Tokyo, Lawrence Berkeley National Laboratory, Leibniz Institut für Astrophysik Potsdam (AIP), Max-Planck-Institut für Astronomie (MPIA Heidelberg), Max-Planck-Institut für Astrophysik (MPA Garching), Max-Planck-Institut für Extraterrestrische Physik (MPE), National Astronomical Observatories of China, New Mexico State University, New York University, University of Notre Dame, Observatário Nacional / MCTI, The Ohio State University, Pennsylvania State University, Shanghai Astronomical Observatory, United Kingdom Participation Group, Universidad Nacional Autónoma de México, University of Arizona, University of Colorado Boulder, University of Oxford, University of Portsmouth, University of Utah, University of Virginia, University of Washington, University of Wisconsin, Vanderbilt University, and Yale University. Land Acknowledgement? This paper includes data collected by the Kepler mission and obtained from the MAST data archive at the Space Telescope Science Institute (STScI). Funding for the Kepler mission is provided by the NASA Science Mission Directorate. STScI is operated by the Association of Universities for Research in Astronomy, Inc., under NASA contract NAS 5–26555.

Software: Python 3 (Van Rossum & Drake 2009), numpy (Harris et al. 2020), matplotlib Hunter (2007), pandas (Wes McKinney 2010), Astropy (Astropy Collaboration et al. 2013, 2018), mw_plot (https://milkyway-plot.readthedocs.io/en/latest/)

Facilities: Du Pont (APOGEE), Sloan (APOGEE), 2MASS, Kepler, K2

REFERENCES

Abdurro'uf, Accetta, K., Aerts, C., et al. 2021, arXiv e-prints, arXiv:2112.02026. https://arxiv.org/abs/2112.02026

Anders, F., Chiappini, C., Minchev, I., et al. 2017, A&A, 600, A70, doi: 10.1051/0004-6361/201629363

Astropy Collaboration, Robitaille, T. P., Tollerud, E. J., et al. 2013, A&A, 558, A33, doi: 10.1051/0004-6361/201322068

Astropy Collaboration, Price-Whelan, A. M., Sipőcz, B. M., et al. 2018, AJ, 156, 123, doi: 10.3847/1538-3881/aabc4f

Auvergne, M., Bodin, P., Boisnard, L., et al. 2009, A&A, 506, 411, doi: 10.1051/0004-6361/200810860

Baglin, A., Auvergne, M., Boisnard, L., et al. 2006, in 36th COSPAR Scientific Assembly, Vol. 36, 3749

Beaton, R. L., Oelkers, R. J., Hayes, C. R., et al. 2021, AJ, 162, 302, doi: 10.3847/1538-3881/ac260c

Bedding, T. R., Huber, D., Stello, D., et al. 2010, ApJL, 713, L176, doi: 10.1088/2041-8205/713/2/L176

Beers, T. C., & Christlieb, N. 2005, ARA&A, 43, 531, doi: 10.1146/annurev.astro.42.053102.134057

Belokurov, V., Erkal, D., Evans, N. W., Koposov, S. E., & Deason, A. J. 2018, Monthly Notices of the Royal Astronomical Society, 478, 611

Bensby, T., Feltzing, S., & Lundström, I. 2003, A&A, 410, 527, doi: 10.1051/0004-6361:20031213

Besla, G., Kallivayalil, N., Hernquist, L., et al. 2007, ApJ, 668, 949, doi: 10.1086/521385

Blanton, M. R., Bershady, M. A., Abolfathi, B., et al. 2017, AJ, 154, 28, doi: 10.3847/1538-3881/aa7567

Bonaca, A., Conroy, C., Cargile, P. A., et al. 2020, ApJL, 897, L18, doi: 10.3847/2041-8213/ab9caa

Borucki, W. J., Koch, D., Basri, G., et al. 2010, Science, 327, 977, doi: 10.1126/science.1185402

Bovy, J. 2015, ApJS, 216, 29, doi: 10.1088/0067-0049/216/2/29

Bowen, I. S., & Vaughan, A. H., J. 1973, ApOpt, 12, 1430, doi: 10.1364/AO.12.001430

Brown, T. M., Gilliland, R. L., Noyes, R. W., & Ramsey, L. W. 1991, ApJ, 368, 599

Buder, S., Sharma, S., Kos, J., et al. 2021, MNRAS, 506, 150

Burbidge, E. M., Burbidge, G. R., Fowler, W. A., & Hoyle, F. 1957, Rev. Mod. Phys., 29, 547

Callingham, T. M., Cautun, M., Deason, A. J., et al. 2022, MNRAS, 513, 4107, doi: 10.1093/mnras/stac1145

Chiappini, C., Matteucci, F., & Gratton, R. 1997, ApJ, 477, 765, doi: 10.1086/303726

Chiappini, C., Anders, F., Rodrigues, T. S., et al. 2015, A&A, 576, L12, doi: 10.1051/0004-6361/201525865

Choi, J., Dotter, A., Conroy, C., et al. 2016, ApJ, 823, 102, doi: 10.3847/0004-637X/823/2/102

Cirasuolo, M., Afonso, J., Carollo, M., et al. 2014, in Society of Photo-Optical Instrumentation Engineers (SPIE) Conference Series, Vol. 9147, Ground-based and Airborne Instrumentation for Astronomy V, ed. S. K. Ramsay, I. S. McLean, & H. Takami, 91470N

Clarke, A. J., Debattista, V. P., Nidever, D. L., et al. 2019, MNRAS, 484, 3476, doi: 10.1093/mnras/stz104

Cox, J. P., & Giuli, R. T. 1968, Principles of stellar structure (Gordon and Breach)

Cui, X.-Q., Zhao, Y.-H., Chu, Y.-Q., et al. 2012, Research in Astronomy and Astrophysics, 12, 1197, doi: 10.1088/1674-4527/12/9/003

Dalton, G., Trager, S., Abrams, D. C., et al. 2020, in Society of Photo-Optical Instrumentation Engineers (SPIE) Conference Series, Vol. 11447, Society of Photo-Optical Instrumentation Engineers (SPIE) Conference Series, 1144714

de Jong, R. S., Bellido-Tirado, O., Chiappini, C., et al. 2012, in Society of Photo-Optical Instrumentation Engineers (SPIE) Conference Series, Vol. 8446, Ground-based and Airborne Instrumentation for Astronomy IV, ed. I. S. McLean, S. K. Ramsay, & H. Takami, 84460T

De Ridder, J., Barban, C., Baudin, F., et al. 2009, Nature, 459, 398, doi: 10.1038/nature08022

Dotter, A. 2016, ApJS, 222, 8, doi: 10.3847/0067-0049/222/1/8

Dotter, A., Chaboyer, B., Jevremović, D., et al. 2008, ApJS, 178, 89, doi: 10.1086/589654

El-Badry, K., Rix, H.-W., & Heintz, T. M. 2021, MNRAS, 506, 2269

Epstein, C. R., Elsworth, Y. P., Johnson, J. A., et al. 2014, ApJL, 785, L28, doi: 10.1088/2041-8205/785/2/L28

Font, A. S., McCarthy, I. G., Crain, R. A., et al. 2011, MNRAS, 416, 2802, doi: 10.1111/j.1365-2966.2011.19227.x

Forbes, D. A. 2020, MNRAS, 493, 847, doi: 10.1093/mnras/staa245

Freeman, K., & Bland-Hawthorn, J. 2002, ARA&A, 40, 487, doi: 10.1146/annurev.astro.40.060401.093840

Fuhrmann, K. 1998, A&A, 338, 161

Gaia Collaboration, Prusti, T., de Bruijne, J. H. J., et al. 2016, A&A, 595, A1, doi: 10.1051/0004-6361/201629272

Gaia Collaboration, Brown, A. G. A., Vallenari, A., et al. 2018, A&A, 616, A1, doi: 10.1051/0004-6361/201833051

Gaia Collaboration, Vallenari, A., Brown, A. G. A., et al. 2023, A&A, 674, A1, doi: 10.1051/0004-6361/202243940

García Pérez, A. E., Allende Prieto, C., Holtzman, J. A., et al. 2016, AJ, 151, 144

Gilmore, G., Wyse, R. F. G., & Kuijken, K. 1989, ARA&A, 27, 555, doi: 10.1146/annurev.aa.27.090189.003011

Girardi, L. 2016, ARA&A, 54, 95, doi: 10.1146/annurev-astro-081915-023354

González Hernández, J. I., & Bonifacio, P. 2009, A&A, 497, 497, doi: 10.1051/0004-6361/200810904

Gould, A., Huber, D., Penny, M., & Stello, D. 2015, Journal of Korean Astronomical Society, 48, 93, doi: 10.5303/JKAS.2015.48.2.93

Gould, A., Huber, D., & Stello, D. 2016, Journal of Korean Astronomical Society, 49, 9, doi: 10.5303/JKAS.2016.49.1.9

Grunblatt, S. K., Zinn, J. C., Price-Whelan, A. M., et al. 2021, ApJ, 916, 88, doi: 10.3847/1538-4357/ac0532

Gunn, J. E., Siegmund, W. A., Mannery, E. J., et al. 2006, AJ, 131, 2332

Harris, C. R., Millman, K. J., van der Walt, S. J., et al. 2020, Nature, 585, 357, doi: 10.1038/s41586-020-2649-2

Hayden, M. R., Recio-Blanco, A., de Laverny, P., Mikolaitis, S., & Worley, C. C. 2017, A&A, 608, L1, doi: 10.1051/0004-6361/201731494

Haywood, M., Di Matteo, P., Lehnert, M., et al. 2018, A&A, 618, A78

Haywood, M., Di Matteo, P., Lehnert, M. D., Katz, D., & Gómez, A. 2013, A&A, 560, A109, doi: 10.1051/0004-6361/201321397

Haywood, M., Lehnert, M. D., Di Matteo, P., et al. 2016, A&A, 589, A66

Helmi, A., Babusiaux, C., Koppelman, H. H., et al. 2018, Nature, 563, 85, doi: 10.1038/s41586-018-0625-x

Helmi, A., & de Zeeuw, P. T. 2000, MNRAS, 319, 657, doi: 10.1046/j.1365-8711.2000.03895.x

Holtzman, J. A., Shetrone, M., Johnson, J. A., et al. 2015, AJ, 150, 148, doi: 10.1088/0004-6256/150/5/148

Holtzman, J. A., Hasselquist, S., Shetrone, M., et al. 2018, AJ, 156, 125, doi: 10.3847/1538-3881/aad4f9

Hon, M., Kuszlewicz, J. S., Huber, D., Stello, D., & Reyes, C. 2022, arXiv e-prints, arXiv:2208.06478

Hon, M., Huber, D., Kuszlewicz, J. S., et al. 2021, ApJ, 919, 131

Howell, M., Campbell, S. W., Stello, D., & De Silva, G. M. 2022, MNRAS, 515, 3184

Howell, S. B., Sobeck, C., Haas, M., et al. 2014, PASP, 126, 398, doi: 10.1086/676406

Huber, D., Stello, D., Bedding, T. R., et al. 2009, Communications in Asteroseismology, 160, 74, doi: 10.48550/arXiv.0910.2764

Huber, D., Bryson, S. T., Haas, M. R., et al. 2016, ApJS, 224, 2, doi: 10.3847/0067-0049/224/1/2

Hunter, J. D. 2007, Computing in Science & Engineering, 9, 90, doi: 10.1109/MCSE.2007.55

Ibata, R. A., Gilmore, G., & Irwin, M. J. 1994, Nature, 370, 194, doi: 10.1038/370194a0

Imig, J., Holtzman, J. A., Yan, R., et al. 2022, AJ, 163, 56, doi: 10.3847/1538-3881/ac3ca7

Jönsson, H., Holtzman, J. A., Allende Prieto, C., et al. 2020, AJ, 160, 120, doi: 10.3847/1538-3881/aba592

Kallinger, T., Beck, P. G., Stello, D., & Garcia, R. A. 2018, A&A, 616, A104, doi: 10.1051/0004-6361/201832831

Khan, S., Miglio, A., Willett, E., et al. 2023, arXiv e-prints, arXiv:2304.07158

Kippenhahn, R., Weigert, A., & Weiss, A. 2013, Stellar Structure and Evolution (Springer), doi: 10.1007/978-3-642-30304-3

Kjeldsen, H., & Bedding, T. R. 1995, A&A, 293, 87. https://arxiv.org/abs/astro-ph/9403015

Koppelman, H. H., Helmi, A., Massari, D., Price-Whelan, A. M., & Starkenburg, T. K. 2019, A&A, 631, L9, doi: 10.1051/0004-6361/201936738

Kruijssen, J. M. D., Pfeffer, J. L., Reina-Campos, M., Crain, R. A., & Bastian, N. 2019, MNRAS, 486, 3180, doi: 10.1093/mnras/sty1609

Laureijs, R., Amiaux, J., Arduini, S., et al. 2011, arXiv e-prints, arXiv:1110.3193. https://arxiv.org/abs/1110.3193

Lee, D. M., Johnston, K. V., Sen, B., & Jessop, W. 2015, ApJ, 802, 48, doi: 10.1088/0004-637X/802/1/48

Lian, J., Thomas, D., Maraston, C., et al. 2020, MNRAS, 494, 2561, doi: 10.1093/mnras/staa867

Limberg, G., Queiroz, A. B. A., Perottoni, H. D., et al. 2023, ApJ, 946, 66, doi: 10.3847/1538-4357/acb694

Lindegren, L., Bastian, U., Biermann, M., et al. 2021, A&A, 649, A4, doi: 10.1051/0004-6361/202039653

Mackereth, J. T., Crain, R. A., Schiavon, R. P., et al. 2018, MNRAS, 477, 5072, doi: 10.1093/mnras/sty972

Mackereth, J. T., Bovy, J., Leung, H. W., et al. 2019a, MNRAS, 489, 176, doi: 10.1093/mnras/stz1521

Mackereth, J. T., Schiavon, R. P., Pfeffer, J., et al. 2019b, MNRAS, 482, 3426

Mackereth, J. T., Miglio, A., Elsworth, Y., et al. 2020, arXiv e-prints, arXiv:2012.00140

—. 2021, MNRAS, 502, 1947, doi: 10.1093/mnras/stab098

Majewski, S. R., Schiavon, R. P., Frinchaboy, P. M., et al. 2017, AJ, 154, 94, doi: 10.3847/1538-3881/aa784d

Marrese, P. M., Marinoni, S., Fabrizio, M., & Altavilla, G. 2019, A&A, 621, A144, doi: 10.1051/0004-6361/201834142

Massari, D., Koppelman, H. H., & Helmi, A. 2019, A&A, 630, L4, doi: 10.1051/0004-6361/201936135

Matsuno, T., Aoki, W., Casagrande, L., et al. 2021, ApJ, 912, 72, doi: 10.3847/1538-4357/abeab2

Mészáros, S., Holtzman, J., García Pérez, A. E., et al. 2013, AJ, 146, 133, doi: 10.1088/0004-6256/146/5/133

Miglio, A., Montalbàn, J., Baudin, F., et al. 2009, A&A, 503, L21, doi: 10.1051/0004-6361/200912822

Miglio, A., Brogaard, K., Stello, D., et al. 2012, MNRAS, 419, 2077

Miglio, A., Chaplin, W. J., Brogaard, K., et al. 2016, MNRAS, 461, 760

Miglio, A., Chiappini, C., Mosser, B., et al. 2017, Astronomische Nachrichten, 338, 644, doi: 10.1002/asna.201713385

Miglio, A., Chiappini, C., Mackereth, J. T., et al. 2021, A&A, 645, A85

Montalbán, J., Mackereth, J. T., Miglio, A., et al. 2021, Nature Astronomy, 5, 640, doi: 10.1038/s41550-021-01347-7

Mosser, B., Gehan, C., Belkacem, K., et al. 2018, A&A, 618, A109, doi: 10.1051/0004-6361/201832777

Mosser, B., Dziembowski, W. A., Belkacem, K., et al. 2013, A&A, 559, A137, doi: 10.1051/0004-6361/201322243

Nidever, D. L., Bovy, J., Bird, J. C., et al. 2014, ApJ, 796, 38, doi: 10.1088/0004-637X/796/1/38

Nidever, D. L., Holtzman, J. A., Allende Prieto, C., et al. 2015, AJ, 150, 173, doi: 10.1088/0004-6256/150/6/173

Ochsenbein, F., Bauer, P., & Marcout, J. 2000, A&AS, 143, 23, doi: 10.1051/aas:2000169

Pérez-Villegas, A., Barbuy, B., Kerber, L. O., et al. 2020, MNRAS, 491, 3251, doi: 10.1093/mnras/stz3162

Pinsonneault, M. H., Elsworth, Y., Epstein, C., et al. 2014, ApJS, 215, 19, doi: 10.1088/0067-0049/215/2/19

Pinsonneault, M. H., Elsworth, Y. P., Tayar, J., et al. 2018, ApJS, 239, 32, doi: 10.3847/1538-4365/aaebfd

Price-Whelan, A., Sipocz, B., Major, S., & Oh, S. 2017, adrn/gala: v0.2.1, doi: 10.5281/zenodo.833339

Price-Whelan, A., Sipőcz, B., Wagg, T., et al. 2022, adrn/gala: v1.6.1, v1.6.1, Zenodo, doi: 10.5281/zenodo.7299506

Price-Whelan, A. M. 2017, The Journal of Open Source Software, 2

Prochaska, J. X., Naumov, S. O., Carney, B. W., McWilliam, A., & Wolfe, A. M. 2000, AJ, 120, 2513, doi: 10.1086/316818

Queiroz, A. B. A., Chiappini, C., Perez-Villegas, A., et al. 2021, A&A, 656, A156, doi: 10.1051/0004-6361/202039030

Rauer, H., Catala, C., Aerts, C., et al. 2014, Experimental Astronomy, 38, 249, doi: 10.1007/s10686-014-9383-4

Rendle, B. M., Miglio, A., Chiappini, C., et al. 2019, MNRAS, 490, 4465

Ricker, G. R., Winn, J. N., Vanderspek, R., et al. 2014, in Society of Photo-Optical Instrumentation Engineers (SPIE) Conference Series, Vol. 9143, Space Telescopes and Instrumentation 2014: Optical, Infrared, and Millimeter Wave, ed. J. Oschmann, Jacobus M., M. Clampin, G. G. Fazio, & H. A. MacEwen, 914320, doi: 10.1117/12.2063489

Rybizki, J., Green, G. M., Rix, H.-W., et al. 2022, MNRAS, 510, 2597

Santana, F. A., Beaton, R. L., Covey, K. R., et al. 2021, AJ, 162, 303, doi: 10.3847/1538-3881/ac2cbc

Schönrich, R., & Aumer, M. 2017, MNRAS, 472, 3979

Schönrich, R., & Binney, J. 2009, MNRAS, 396, 203, doi: 10.1111/j.1365-2966.2009.14750.x

Schönrich, R., McMillan, P., & Eyer, L. 2019, MNRAS, 487, 3568

Sellwood, J. A., & Binney, J. J. 2002, MNRAS, 336, 785, doi: 10.1046/j.1365-8711.2002.05806.x

Sharma, S., Bland-Hawthorn, J., Johnston, K. V., & Binney, J. 2011, ApJ, 730, 3, doi: 10.1088/0004-637X/730/1/3

Sharma, S., Hayden, M. R., & Bland-Hawthorn, J. 2021, MNRAS, 507, 5882, doi: 10.1093/mnras/stab2015

Sharma, S., Stello, D., Bland-Hawthorn, J., Huber, D., & Bedding, T. R. 2016, ApJ, 822, 15, doi: 10.3847/0004-637X/822/1/15

Sharma, S., Stello, D., Huber, D., Bland-Hawthorn, J., & Bedding, T. R. 2017, ApJ, 835, 163, doi: 10.3847/1538-4357/835/2/163

Sharma, S., Stello, D., Zinn, J. C., et al. 2022, MNRAS, doi: 10.1093/mnras/stac2031

Silva Aguirre, V., Bojsen-Hansen, M., Slumstrup, D., et al. 2018, MNRAS, 475, 5487

Simpson, C. M., Gargiulo, I., Gómez, F. A., et al. 2019, MNRAS, 490, L32, doi: 10.1093/mnrasl/slz142

Soderblom, D. R. 2010, ARA&A, 48, 581

Spergel, D., Gehrels, N., Baltay, C., et al. 2015, arXiv e-prints, arXiv:1503.03757. https://arxiv.org/abs/1503.03757

Stello, D., & Sharma, S. 2022, Research Notes of the American Astronomical Society, 6, 168, doi: 10.3847/2515-5172/ac8b12

Stello, D., Huber, D., Bedding, T. R., et al. 2013, ApJL, 765, L41, doi: 10.1088/2041-8205/765/2/L41

Stello, D., Compton, D. L., Bedding, T. R., et al. 2014, ApJL, 788, L10, doi: 10.1088/2041-8205/788/1/L10

Stello, D., Huber, D., Sharma, S., et al. 2015, ApJL, 809, L3, doi: 10.1088/2041-8205/809/1/L3

Stello, D., Zinn, J., Elsworth, Y., et al. 2017, VizieR Online Data Catalog, J/ApJ/835/83

Suda, T., Katsuta, Y., Yamada, S., et al. 2008, PASJ, 60, 1159, doi: 10.1093/pasj/60.5.1159

Tailo, M., Corsaro, E., Miglio, A., et al. 2022, A&A, 662, L7

Tayar, J., Beck, P. G., Pinsonneault, M. H., García, R. A., & Mathur, S. 2019, ApJ, 887, 203, doi: 10.3847/1538-4357/ab558a

Timmes, F. X., Woosley, S. E., & Weaver, T. A. 1995, ApJS, 98, 617

Torra, F., Castañeda, J., Fabricius, C., et al. 2021, A&A, 649, A10, doi: 10.1051/0004-6361/202039637

Valentini, M., Chiappini, C., Bossini, D., et al. 2019, A&A, 627, A173

Van Rossum, G., & Drake, F. L. 2009, Python 3 Reference Manual (Scotts Valley, CA: CreateSpace)

Venn, K. A., Irwin, M., Shetrone, M. D., et al. 2004, AJ, 128, 1177, doi: 10.1086/422734

Viani, L. S., Basu, S., Chaplin, W. J., Davies, G. R., & Elsworth, Y. 2017, ApJ, 843, 11

Warfield, J. T., Zinn, J. C., Pinsonneault, M. H., et al. 2021, AJ, 161, 100, doi: 10.3847/1538-3881/abd39d

Weinberg, D. H., Andrews, B. H., & Freudenburg, J. 2017, ApJ, 837, 183, doi: 10.3847/1538-4357/837/2/183

Wes McKinney. 2010, in Proceedings of the 9th Python in Science Conference, ed. Stéfan van der Walt & Jarrod Millman, 56 – 61, doi: 10.25080/Majora-92bf1922-00a

White, T. R., Bedding, T. R., Stello, D., et al. 2011, ApJ, 743, 161, doi: 10.1088/0004-637X/743/2/161

Wilson, J. C., Hearty, F. R., Skrutskie, M. F., et al. 2019, PASP, 131, 055001

Wolniewicz, L. M., Berger, T. A., & Huber, D. 2021, AJ, 161, 231, doi: 10.3847/1538-3881/abee1d

Wu, Y., Xiang, M., Bi, S., et al. 2017, Monthly Notices of the Royal Astronomical Society, 475, 3633, doi: 10.1093/mnras/stx3296

Yu, J., Huber, D., Bedding, T. R., et al. 2018, ApJS, 236, 42

Zasowski, G., Cohen, R. E., Chojnowski, S. D., et al. 2017, AJ, 154, 198

Zinn, J. C., Huber, D., Pinsonneault, M. H., & Stello, D. 2017, ApJ, 844, 166

Zinn, J. C., Pinsonneault, M. H., Bildsten, L., & Stello, D. 2023, arXiv e-prints, arXiv:2308.09854, doi: 10.48550/arXiv.2308.09854

Zinn, J. C., Pinsonneault, M. H., Huber, D., et al. 2019a, ApJ, 885, 166

—. 2019b, ApJ, 885, 166, doi: 10.3847/1538-4357/ab44a9

Zinn, J. C., Stello, D., Elsworth, Y., et al. 2020, ApJS, 251, 23, doi: 10.3847/1538-4365/abbee3

—. 2022, ApJ, 926, 191, doi: 10.3847/1538-4357/ac2c83